Studies Of Rare-Earth Doping On α-Fe_2O_3 Nanoparticles

Dissertation

Submitted in partial fulfillment for the Degree of

MASTER OF TECHNOLOGY
In
NANOSCIENCE and TECHNOLOGY

GAURAV GOYAL
2K09/NST/02

DEPARTMENT OF APPLIED PHYSICS
(IN ASSOCIATION WITH NATIONAL PHYSICAL LABORATORY)

DELHI TECHNOLOGICAL UNIVERSITY
(Formerly Delhi College of Engineering)
2011

Studies of rare-earth doping on α-Fe_2O_3 nanoparticles

Dissertation

Submitted in Partial Fulfillment for the Degree of

MASTER OF TECHNOLOGY
In
NANOSCIENCE and TECHNOLOGY

Submitted by

GAURAV GOYAL
2K09/NST/02

Under the Supervision of

Dr. ANJANA DOGRA
Scientist
National Physical Laboratory

DEPARTMENT OF APPLIED PHYSICS
(IN ASSOCIATION WITH NATIONAL PHYSICAL LABORATORY)

DELHI TECHNOLOGICAL UNIVERSITY

(Formerly Delhi College of Engineering)

Main Bawana Road, Shahabad Daulatpur, New Delhi – 110042

2011

CERTIFICATE

This is to certify that dissertation titled **"Studies of rare-earth doping on α-Fe_2O_3 nanoparticles"** is submitted by **Gaurav Goyal** (2K09/NST/02) towards the partial fulfillment of M.Tech Degree in Nanoscience and Technology under the supervision of **Dr. Anjana Dogra**. This Work was performed at **National Physical Laboratory**, Delhi. The work has not been submitted elsewhere for the award of any degree.

Dr. Anjana Dogra
Scientist 'C'
National Physical Laboratory
Delhi

Dr. Rajiv Chopra
Head, HRD
National Physical Laboratory
Delhi

Date_____ _____

Place_____ _____

(Examiner)

ACKNOWLEDGEMENTS

Completing a task of this dimension could never be a one-man effort. It is often the result of invaluable contribution of number of individuals in a direct or indirect way that helps in the scripting of a success.

First of all I would like to thank Dr. R.C Budhani, Director and HRD Head of National Physical Laboratory, for allowing me to do my M.Tech research Project at this premier research institute.

The successful culmination of our effort remind me of my indebtedness towards my venerated guide Dr. Anjana Dogra, Quantum Phenomenon and Applications Division, National Physical Laboratory, Delhi for her invaluable guidance and encouragement during the entire project. I had no previous research experience in "Nano Science". She taught me how to come up with ideas regarding research and helped me even with mundane lab work, like the setting up of bench apparatus. Her endless passion towards science has made me a better researcher.

I sincerely thank Dr. V. Siruguri, Dr. S. Rayaprol and Dr. S. D. Kaushik from UGC-DAE Consortium for Scientific Research, BARC Campus, Mumbai for Neutron diffraction experiments carried out on FCD at Dhruva reactor-BARC, Mumbai. My sense of obligations is due to Dr. Rayaprol for also helping me with SQUID measurements and neutron analysis that provides a meaningful direction to the present study.

With profound appreciation and sincere indebtedness, I express my deep gratitude to Dr. R.K Sinha, HOD, Department of Physics, DTU for granting me the permission to do project work at NPL. His constant encouragement and interest was instrumental in the completion of project. I am also thankful to all of my faculty members of the department for their valuable suggestions time to time.

Finally, yet importantly, I would like to express my heartfelt thanks to my beloved parents for their blessings, my friends/classmates for their help and wishes for the successful completion of this project.

Help and cooperation received from any other quarters not acknowledged above is purely unintentional and I apologize for the same.

LIST OF FIGURES

Annexure

LIST OF TABLES

TABLE OF CONTENTS

Chapter 1

Introduction

1.1 Magnetic Nanoparticle

In the last two decades, new terms with the prefix `nano' have rushed into the scientific vocabulary - nanoparticle, nanostructure, nanotechnology, nanomaterial, nanocluster, nanochemistry, nanocolloids, nanoreactor and so on. The enhanced interest of the researchers in nanoobjects is due to the discovery of unusual physical and chemical properties of these objects, which is related to manifestation of so-called `quantum size effects.' A key reason for the change in the physical and chemical properties of small particles is the increased fraction of the `surface' atoms, which occur under conditions (coordination number, symmetry of the local environment, etc.) differing from those of the bulk atoms.

Currently, unique physical properties of nanoparticles are under intensive research [1]. A special place belongs to the magnetic properties in which the difference between a massive (bulk) material and a nanomaterial is especially pronounced. In particular, it was shown that magnetisation (per atom) and the magnetic anisotropy of nanoparticles can be much greater than those of a bulk specimen, while differences in the Curie (T_C) or Neel (T_N) temperatures between nanoparticle and the corresponding microscopic phases reach hundreds of degrees. In addition, magnetic nanomaterials were found to possess a number of unusual properties - giant magnetoresistance, abnormally high magnetocaloric effect, and so on. The magnetic properties of nanoparticles are determined by many factors, the key of these including the chemical composition, the type and the degree of defectiveness of the crystal lattice, the particle size and shape, the morphology, the interaction of the particle with the surrounding matrix and the neighboring particles.

The last years have seen changes in the development of magnetic nanomaterials, which can be called revolutionary. Magnetic nanoparticles are abundant in nature and are found in many biological objects [2]. Magnetic nanomaterials are used in information recording and storage

systems, in new permanent magnets, in magnetic cooling systems, as magnetic sensors, etc. Among the magnetic materials that have found broad practical application in technology, ferromagnets deserve attention. An important characteristic of a ferromagnet is the coercive force (H_c), i.e., the magnetic field strength H corresponding to the point with B=0 on the symmetric hysteresis loop B(H) of the ferromagnet.

In addition to ferromagnets in which the magnetic moments of the atoms are ordered, magnetic spin glasses - systems in which the competition of random magnetic interactions between magnetic moments results in a magnetic disordered state - also find application in technology.

A series of general methods for the nanoparticle synthesis have now been developed as shown in Table 1.1 [3]. Most of them can also be used for the preparation of magnetic particles. An essential feature of their synthesis is the preparation of particles of specified size and shape. The shape control and the possibility of synthesis of anisotropic magnetic structures are especially important.

Synthetic method	Nanoparticle characteristics							
	Size		Shape control	Synthesis	Reaction			Surface capping agents
	Range	Distribution			Temperature	Time	Yield	
Aerosol/vapor (pyrolisys)	5-60 nm	Broad	Good	Complicated, vacuum/ controlled atmosphere	High/ very high	Minutes /hours	Medium	Needed, after reaction
Gas deposition	5-50 nm	Narrow	Good	Complicated, vacuum/ controlled atmosphere	Very high	Minutes	High/ scalable	Needed, after reaction
Sol-gel	3-150 nm	Narrow/ broad	Good	Simple	20-90 °C	Hours/ days	Medium	Needed, during reaction
Co-precipitation	10-50 nm	Broad/ narrow	Poor	Very simple	20-90 °C	Minutes	High/ scalable	Needed, during reaction
Thermal decomposition	2-20 nm	Very narrow	Very good	Complicated, inert atmosphere	100-330 °C	Hours	High/ scalable	Needed, during reaction
Microemulsion	4-15 nm	Narrow	Good	Complicated	20-70 °C	Hours/ days	Low	Needed, during reaction
Hydrothermal	10-150 nm	Narrow	Very good	Simple, high pressure	100 °C -high	Hours/ days	Medium	Needed, during reaction

Table 1.1: Comparison of different synthetic methods to produce MNPs.

The choice of the synthesis process is a fundamental step in obtaining the desired characteristics in the final product. The production of exceedingly pure powders, with small normal particle size and low aggregation and agglomeration, in addition to achieving low production costs and the shortest possible time, are some examples of parameters to be analyzed when choosing a synthesis technique. Although varying in their efficiency levels, most of the available processes do not achieve all these items.

Methods such as solid-state reaction synthesis are carried out at high temperature (>1000^{o}C); consequently, the use of high temperatures during sintering or calcination results in the loss of fine particulates in the obtained product. In the coprecipitation process, the greatest inconvenience is the rigorous control of the pH of the metallic solution. Sol-gel and microemulsion techniques, for instance, involve large amounts of organic solvents or the addition of surfactants during the reaction. Among several nonconventional methods of synthesis to obtain nanostructured ferrites, ***solution combustion synthesis*** **(SCS)** was selected. Through this method, it is possible to obtain a product with high purity, containing fine particles and, in some cases, combined with high surface area. Furthermore, the advantages of this technique are simple experimental procedure, low cost, and very short duration between preparation of the reagents and obtaining the final product. The combustion reaction, exothermic by nature, is self-sustainable, allowing the system to heat quickly, thereby reaching high temperatures, even in the absence of an external heat source. The self-stop mode ensures the crystallinity of the powder, in addition to maintaining the homogeneity and the superior grade of purity [6].

This process involves a self-sustained reaction in homogeneous solution of different oxidizers (e.g., metal nitrates) and fuels (e.g., urea, glycine, hydrazides). This process not only yields nanosize oxide materials but also allows uniform (homogeneous) doping of trace amounts of rare-earth impurity ions in a single step.

Several books [4–7] and reviews [8–13] have been published on this subject in recent years. Specific directions for SHS nanosynthesis were reviewed by Merzhanov et al. [11].

Combustion synthesis is of three following types:

a) **Condensed phase Combustion**: It is a conventional self-propagating high-temperature synthesis (SHS) method for nanoscale materials. In this, initial reactants are in solid state.
b) **Solution-combustion synthesis**: In this, initial reaction medium is aqueous solution.
c) **Gas-phase combustion:** Synthesis of nanoparticles in flame.

1.2 Magnetic properties

If a magnetic material is placed in a magnetic field of strength ***H***, the individual atomic moments in the material contribute to its overall response, the magnetic induction:

$$\boldsymbol{B} = \mu_0(\boldsymbol{H} + \boldsymbol{M}),$$

Where μ_0 is the permeability of free space, and the magnetization $\boldsymbol{M} = \boldsymbol{m}/V$ is the magnetic moment per unit volume, where ***m*** is the magnetic moment on a volume V of the material.

All the materials are magnetic to some extent, with their response depending on their atomic structure and temperature. They may be conveniently classified in terms of their volumetric magnetic susceptibility, χ, where

$$M = \chi.H = C.H/T$$

Where, M is the resulting magnetization, χ is the magnetic susceptibility, T is the absolute temperature, and C is a material-specific Curie constant.

There are various forms of magnetism that arise depending on how the dipoles interact with each other:-

1.2.1 Paramagnetism

Paramagnetism is a form of magnetism that occurs only in the presence of an externally applied magnetic field. Paramagnetic materials have a relative magnetic permeability greater or equal to unity, i.e. a positive magnetic susceptibility, and hence are attracted to magnetic fields. The magnetic moment induced by the applied field is linear in the field strength and rather weak. Unlike ferromagnets, paramagnets do not retain any magnetization in the absence of an externally applied magnetic field, because thermal motion randomizes the spin orientation.

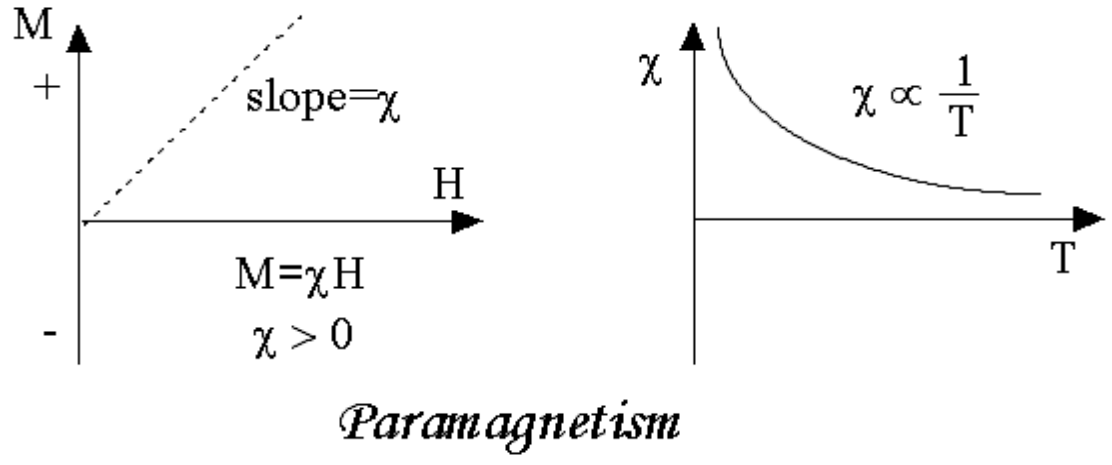

Fig 1.1: M-H and χ-T curve for paramagnetic materials (PM).

1.2.2 Diamagnetism

Diamagnetism is a fundamental property of all matter, although it is usually very weak. It is due to the non-cooperative behavior of orbiting electrons when exposed to an applied magnetic field. Diamagnetic substances are composed of atoms which have no net magnetic moments (ie, all the orbital shells are filled and there are no unpaired electrons). However, when exposed to a field, a negative magnetization is produced and thus the susceptibility is negative. If we plot M vs H, we see:

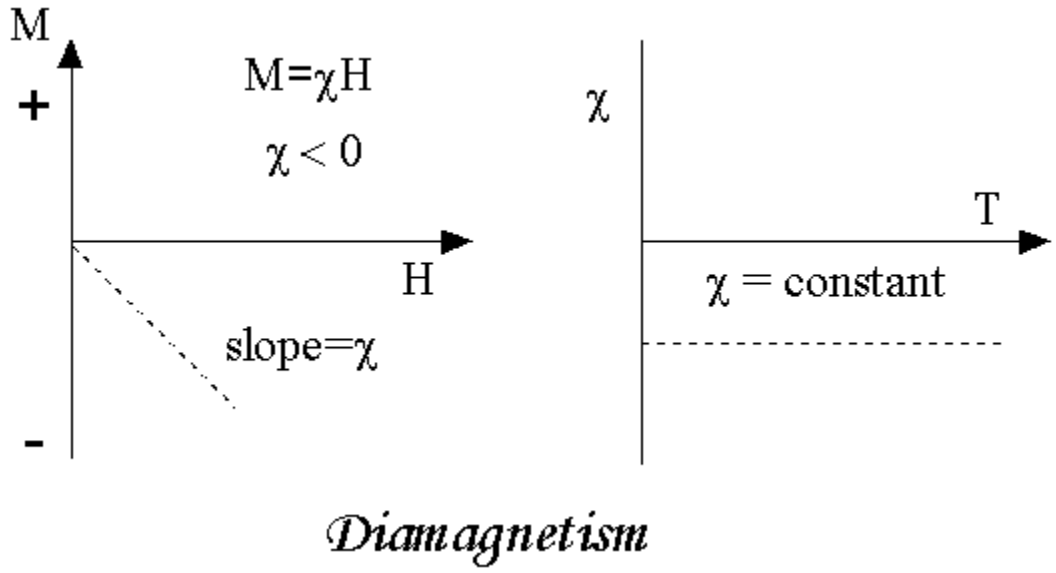

Fig 1.2: M-H and χ-T curve for Diamagnetic materials (DM).

1.2.3 Ferromagnetism

Ferromagnetism is the basic mechanism by which materials can be magnetized by an external magnetic field and which *remain* magnetized after the external field is removed. Unlike paramagnetic materials, the atomic moments in these materials exhibit very strong interactions. These interactions are produced by electronic exchange forces and result in a parallel or antiparallel alignment of atomic moments. Exchange forces are very large, equivalent to a field on the order of 1000 Tesla, or approximately a 100 million times the strength of the earth's field.

The susceptibility in ordered materials depends not just on temperature, but also on ***H***, which gives rise to the characteristic sigmoidal shape of the *M–H* curve, with ***M*** approaching a saturation value at large values of ***H***. Furthermore, in ferromagnetic and ferrimagnetic materials one often sees hysteresis, which is irreversibility in the magnetization process that

is related to the pinning of magnetic domain walls at impurities or grain boundaries within the material, as well as to intrinsic effects such as the magnetic anisotropy crystalline lattice. This gives rise to open ***M–H*** curves, of the called hysteresis loops. The shape of these loops are determined in part by particle size: in large particles (of the order micron size or more) there is a multi-domain ground state which leads to a narrow hysteresis loop since it takes relatively little field energy to make the domain walls move; while in smaller particles there is a single domain ground state which leads to a broad hysteresis loop.

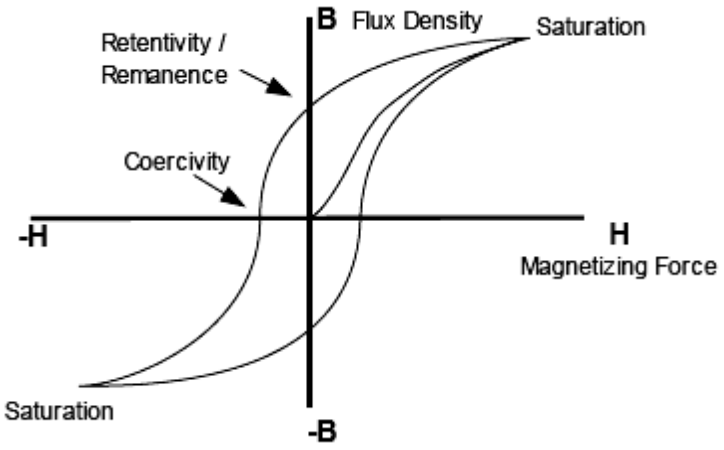

Fig 1.3: Hysteresis curve for ferromagnetic materials.

1.2.4 Superparamagnetism

Superparamagnetism is a form of magnetism, which appears in small ferromagnetic or ferromagnetic nanoparticles. Superparamagnetism behaves in a similar way to paramagnetism, while ferromagnetic materials are used. This means the saturation magnetization of superparamagnetic material can be much higher than normal paramagnetic materials and no remanent magnetization are present without external fields.

Due to superparamagnetism, the magnetic moment of a particle as a whole is free to fluctuate in response to thermal energy while the individual magnetic moments maintain their ordered state relative to each other.

This leads to an anhysteric but still sigmoidal M-H curve as shown in Fig.1.4

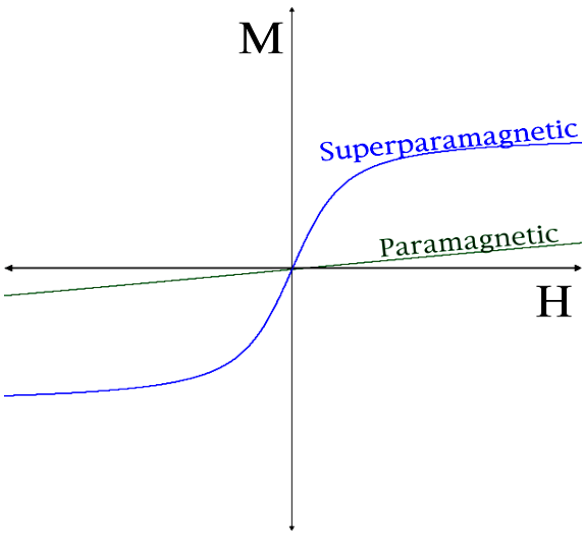

Fig 1.4: *M-H* curve for superparamagnetic and paramagnetic system.

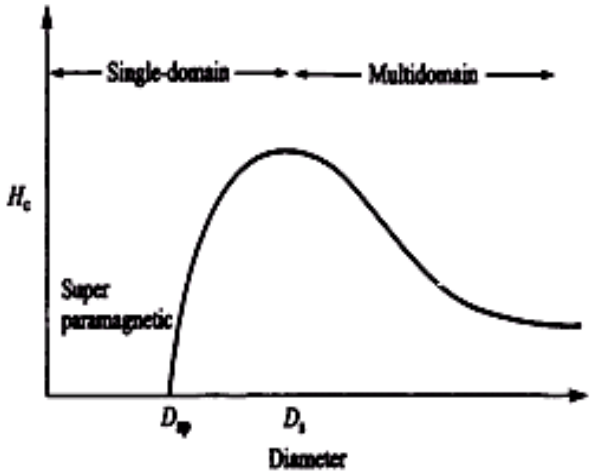

Figure 1.5:-Particle coercivity versus size (~diameter). D_{sp} is the superparamagnetic size; D_s is the single-domain size.

When size of material falls below critical value, they exhibit Superparamagnetism (SPM). For ferric oxide nanoparticle the critical size is 20 nm.

Bulk ferromagnetic materials are generally polycrystalline with each grain consisting of thousands of magnetic domains separated by boundaries called domain walls. Figure 1.6 as the simplest case shows multidomain particle with 90° domain walls. The magnetic domain walls have significant width, generally in the tens to hundreds of nanometers. As the size of a bulk ferromagnet is reduced until it is reached to the domain wall width, particles consist of a single domain that thermodynamically cannot support the formation of a domain wall. This requires magnetization reversal by rotation of the magnetization into the applied field direction.

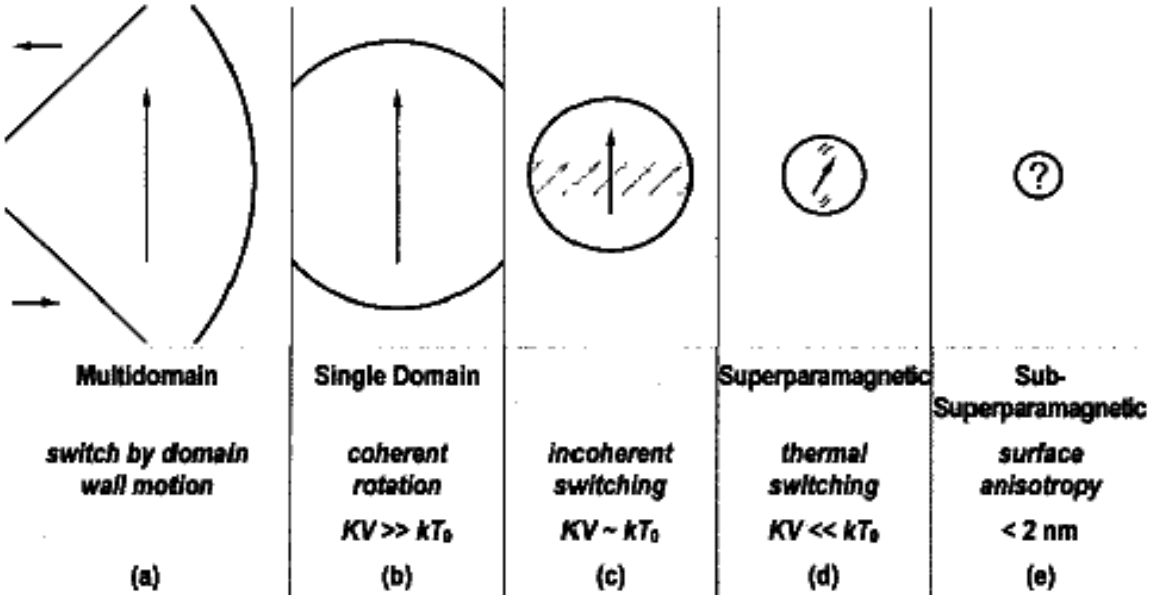

Fig 1.6: Non-interacting particles as function of particle size, indicating magnetization reversal mechanism regimes at isothermal temperature.

Again, the magnetic properties depend on the material type and size, which can be described as the relaxation of the magnetization orientation of each particle by time τ [14, 15].

$$\text{Where,} \quad \tau = \tau_o \exp(E/K_B T)$$

$$\& \qquad E = KV$$

Where, E = thermal energy barrier to moment reversal

$K_B T$ = thermal energy

V = particle volume

K = anisotropic energy density

The term KV measures the energy barrier between two orientations. As the size of the particle decreases to a level where KV becomes comparable to the thermal energy $K_B T$, its magnetization starts to fluctuate from one direction to another. As a result, at this T the overall magnetic moment of this particle is randomized to zero, and the particle is said to be superparamagnetic. (Figure 1.7)

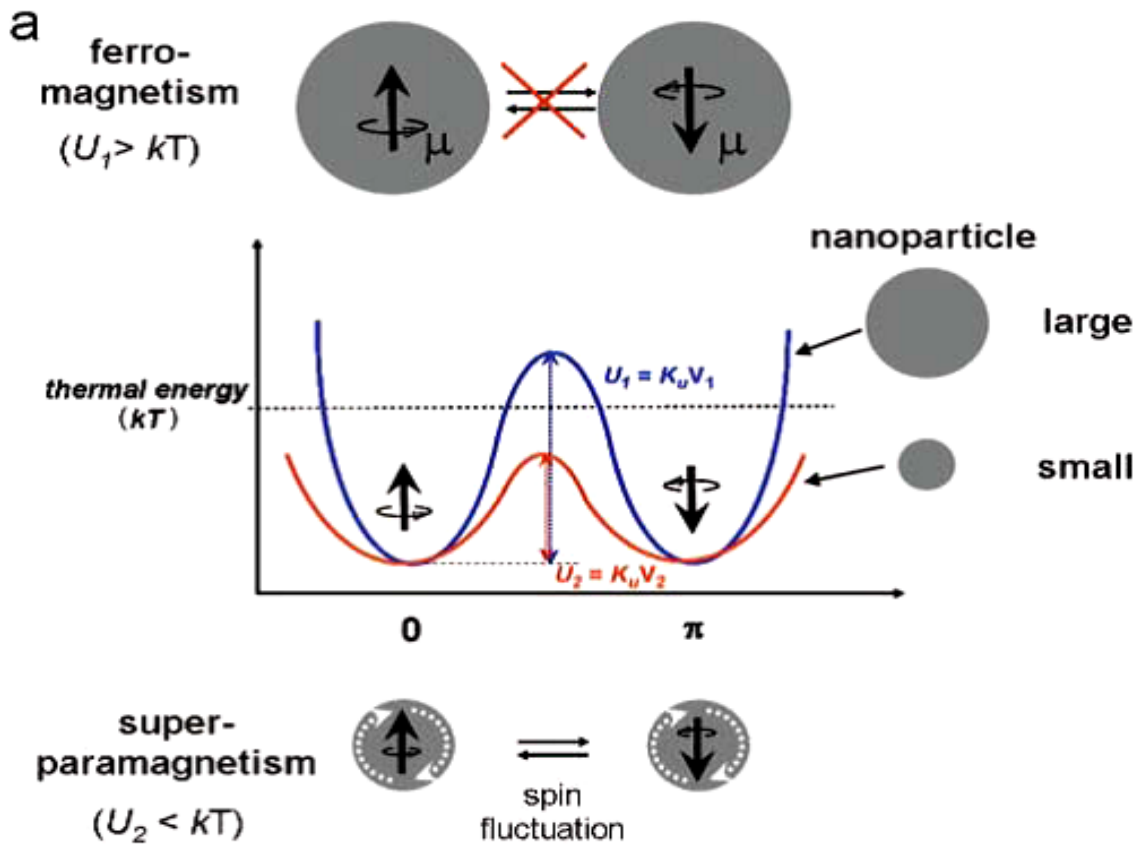

Fig.1.7: Nanoscale transition of magnetic nanoparticles from ferromagnetism to superparamagnetism.

There are two main mechanisms for the magnetization reversal: Spin rotation and Particle rotation, which describe whether the change in direction of the magnetic moment of the particle is due to the reversal of the magnetic spin of the particle or the actual physical rotation of the particle.

The time required for the reversal of the magnetic moment of the particle (spin rotation) is related to the magnetic anisotropy of the material, Neel relaxation time, T_N. The characteristic time for the randomization of the magnetization is mainly due to the thermal motion of the particle known as Brown relaxation time, T_B.

For a superparamagnetic material $T_N << T_B$, which means that the magnetization reversal occurs by rotation of the magnetic axis. The criterion of superparamagetism is regularly assumed considering particles with a relaxation time lower than 100 s.

Magnetic properties of nanometer-sized particles of both ferromagnetic and ferrimagnetic materials have attracted considerable attention in recent years because of their unique properties which make them very appealing both from scientific value of understanding their properties and technological significance of enhancing the performance of the existing materials. Among ferromagnetic materials, iron (III) oxide has gained more importance.

1.3 Iron oxide Nanoparticle

Iron (III) oxide or **ferric oxide** is the inorganic compound with the formula Fe_2O_3. It is one of the three main oxides of iron, the other two being iron (II) oxide (FeO), which is rare, and iron (II, III) oxide (Fe_3O_4), which also occurs naturally as the mineral magnetite.

Iron (III) oxide (Fe_2O_3) has following different forms:-

- alpha phase, hematite (α-Fe_2O_3)
- beta phase, (β-Fe_2O_3)
- gamma phase, maghemite (γ-Fe_2O_3)
- epsilon phase, (ε-Fe_2O_3)

Alpha phase

α-Fe_2O_3 has the rhombohedral, corundum (α-Al_2O_3) structure and is the most common form. It occurs naturally as the mineral hematite which is mined as the main ore of iron. It is antiferromagnetic below ~260 K (Morin transition temperature), and weak ferromagnetic between 260 K and 950 K i.e, Neel temperature [16-17]. It is easy to prepare using both thermal decomposition and precipitation in the liquid phase. Its magnetic

properties are dependent on many factors, e.g. pressure, particle size, and magnetic field intensity.

Beta phase

Cubic face centered, metastable, at temperatures above 500 °C converts to alpha phase. It can be prepared by reduction of hematite by carbon, pyrolysis of iron (III) chloride solution, or thermal decomposition of iron (III) sulfate.

Gamma phase

Cubic, metastable, converts to the alpha phase at high temperatures. Occurs naturally as the mineral maghemite. It is ferromagnetic but ultrafine particles smaller than 10 nanometers are superparamagnetic. It can be prepared by thermal dehydratation of gamma iron (III) oxide-hydroxide, careful oxidation of iron (II, III) oxide. The ultrafine particles can be prepared by thermal decomposition of iron (III) oxalate.

Epsilon phase

Rhombic, shows properties intermediate between alpha and gamma. So far has not been prepared in pure form; it is always mixed with the alpha phase or gamma phases. Material with a high proportion of epsilon phase can be prepared by thermal transformation of the gamma phase. The epsilon phase is metastable, transforming to the alpha phase at between 500 and 750 °C.

Out of various phases **α-Fe_2O_3** has always attracted researchers because of their potential application in catalyst, magnetic recording media, pigments, anticorrosive agents and gas sensors [18-28]. Its non-toxicity, low cost, and relatively good stability are attractive features for specific applications [29]. Recently, great attention has been devoted to the synthesis and characterization of aniferroamagnetic **α-Fe_2O_3 (hematite)** nanoparticles. The magnetic and structural properties of hematite are known to be affected by particle size, degree of crystallinity, pressure and also doping [26]. In particular, these factors are found to be very much size dependent and critically sensitive to the methodologies employed to synthesize them [30]. Several chemical and physical methods were employed to prepare α-Fe_2O_3 nanoparticles. It was reported that α-Fe_2O_3 nanoparticles can be synthesize through sol-gel [23], RF magnetron sputtering method [24], solvothermal method [31], sonochemical synthesis [23], microemulsion technique, forced hydrolysis method [27], hydrothermal approach [28], planetary ball milling, etc. [18].

The resulting physio-chemical properties of nanosized magnetic product obviously depend strongly on the fabrication conditions, especially on material origin, concentration and pH of solution as well as on the mode of thermal treatment used (annealing temperature, atmosphere and rate of heating/cooling).

1.3.1 Crystal Structure of hematite (α-Fe_2O_3)

The crystal structure of hematite is same as that of corundum, Al_2O_3, which can be describes as rhombohedral or hexagonal with the space group R-3c. Hematite is weakly ferromagnetic at room temperature and has a Neel temperature of about 953 K [32]. Below room temperature, Hematite is having another magnetic transition called Morin transition (T_M) by which it changes from weakly ferromagnetic to antiferromagnetic [33]. In between T_M and T_N, hematite is weakly ferroamgnetic and in this state, the spins lie in the basal plane (111) of rhombohedral unit cell slightly canted from antiparallel alignment reulting in weal magnetic moment originating from Dzyaloshinskii-Moriya anisotropic superexchange interaction [34].

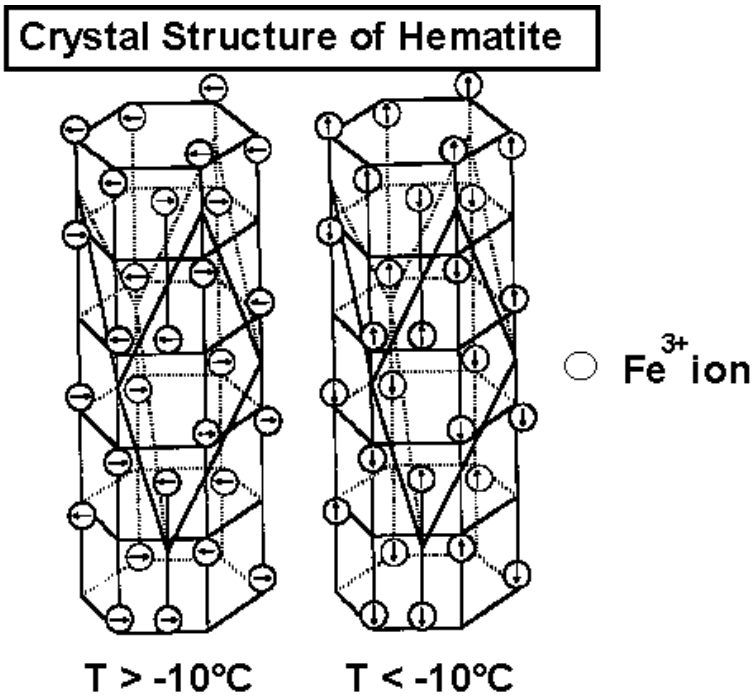

Fig. 1.8: Schematic view depicting crystal structure of hematite.

As shown in Fig. 1.8, above -10°C, the spin moments lie in the c-plane but are slightly canted. This produces a weak spontaneous magnetization within the c-plane (σ_s = 0.4 Am^2/kg).

Below -10°C, the direction of the antiferromagnetism changes and becomes parallel to the c-axis; there is no spin canting and hematite becomes a perfect antiferromagnet. This spin-flop transition is called the **Morin transition (T_M)**.

Fig 1.9 also shows a graph depicting Morin transition temperature and Curie point temperature for hematite.

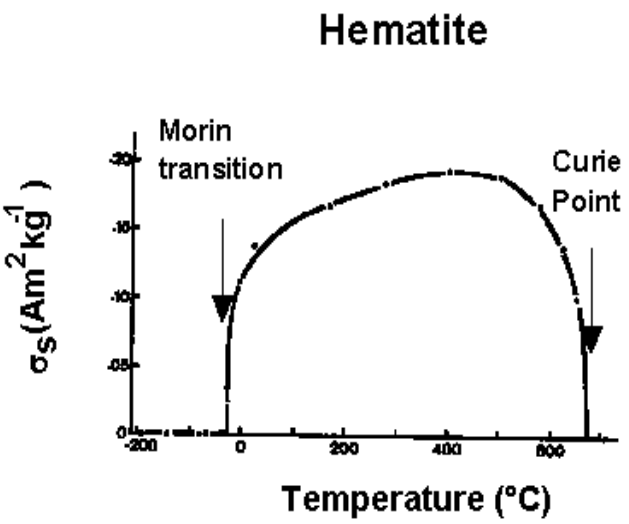

Fig. 1.9: Graph showing Morin transition temperature and Curie point.

1.3.2 Magnetic Structure of α-Fe_2O_3

The magnetic unit cell of α-Fe_2O_3 is suggested to be of the same size as the conventional chemical unit cell as determined by X-ray diffraction. This is a rhombohedral cell of edge length 5.42 A° and rhombohedral angle 55°17', with two iron oxide molecules contained in the unit cell. The innermost two reflections (111) and (100) as shown in Fig1.10, is most interesting and most informative in the neutron pattern.

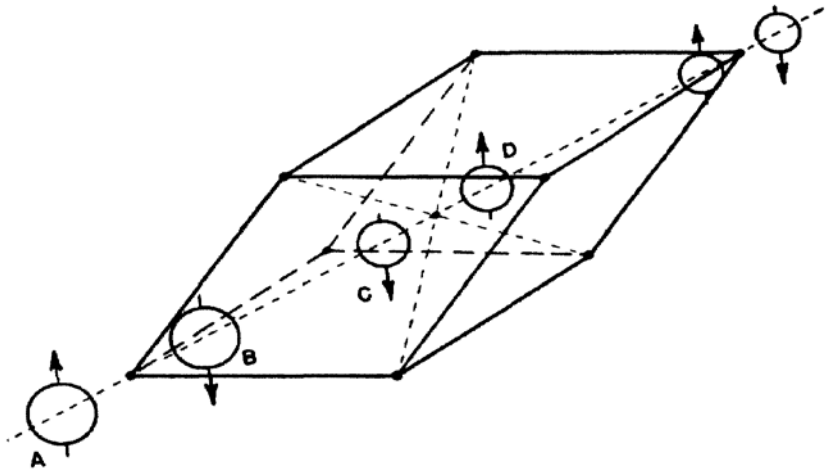

Fig. 1.10: The Magnetic Structure of α-Fe_2O_3 at room temperature. The rhombohedral unit cell containing four unique iron atoms shown as ABCD.

1.4 Application of Iron oxide Nanoparticle

Nanoparticles of iron oxide have applications in information storage, color imaging, bioprocessing, magnetic refrigeration, medical diagnosis and controlled drug delivery and as ferrofluids. Thus, developing new synthetic routes for α-Fe_2O_3 nanoparticles and the investigation of their properties are of great importance. Some of the applications of iron oxide are described as following:-

1.4.1 Cell separations

The separation of cells is achieved by covalently binding of α-Fe_2O_3 nanoparticles to the cells. The bead carrying a specific antibody -usually monoclonal antibodies- on the surface binds selectively the target cell which can then be removed from the suspension with the help of a magnet.

The separated cells has been used for the purging and isolation of cancer cells, studies of HIV and AIDS, isolation of granulocytes, isolation of cells from various tissues stem cells, etc.

1.4.2 Drug delivery

The drug delivery with the help of α-Fe_2O_3 nanoparticles can be achieved by coating the particle by a biocompatible polymer such as PVA or dextran, although inorganic coatings such as silica can also be used. The coating can be functionalized by attaching carboxyl groups, biotin, avidin or other molecules. The molecules then act as attachment points for the coupling of cytotoxic drugs or target antibodies to the carrier complex.

1.4.3 Hyperthermia

Hyperthermia is the treatment of cancer with the help of temperature. In magnetic hyperthermia, the α-Fe_2O_3 nanoparticles are injected in to the target place and heat is provided by applying magnetic field. Magnetic particle hyperthermia is appealing because it offers a way to ensure only the intended target tissue is heated.

Besides this, there are many other applications of magnetic nanoparticles like they can be used for MRI contrast enhancement, catalysis, magnetic recording media, magnetic fluids and environmental remediation [18-28].

1.5 Literature Survey on α-Fe_2O_3

In recent times magnetic nanoparticles (NPs) have been the subject of intense scientific and technological research [35, 36]. Iron oxide NPs have been extensively studied by a number of experimental techniques such as magnetic measurements [37-51], Mossbauer spectroscopy [39-45, 51, 37-44], electron paramagnetic resonance (EPR) [48] and neutron diffraction [52]. It is revealed that the magnetic properties of NPs are extremely sensitive to interparticle interactions.

Of six known crystalline phases of iron oxide, γ-Fe_2O_3 (maghemite) [53, 54] and α-Fe_2O_3 (hematite) [55, 56] have been most extensively studied. In particular, maghemite has been widely used in magnetic recording systems and catalysis [57, 58], whereas hematite has been used in pigments, catalytic reactions and as an anticorrosive agent [60].

Hematite crystallizes in the trigonal system, space group R-3c [61].The magnetic properties of α-Fe_2O_3 have interested researchers for many years, particularly after Morin [62, 63] reported a phase transition from weakly ferromagnetic to an antiferromagnetic (AFM) state on cooling below the Morin temperature (T_M = 260 K). A neutron diffraction study by Shull *et. al* [32] showed that α-Fe_2O_3 is, in essence, an AFM below its Neel temperature T_N = 960K, and that the WFM → *AFM* transition was in fact a temperature-driven spin-flop (SF). Below T_M, spins are oriented in antiparallel directions along the trigonal [111] axis (c axis), and the material behaves as a uniaxial AFM [64]. Above T_M, spins show slight canting (~ 1 min of arc) with respect to the basal [111] plane [65, 66] which give rise to small net weak ferromagnetic moment. In the AFM state SF transitions were subsequently observed by several investigators.

As the size of the hematite particle decreases and enters the nanometre scale, the magnetic properties change and new phenomena appear. Consequently, nanoparticle hematite is an even more interesting material for fundamental research because it can display three critical temperatures: the Neel temperature (T_N), the Morin temperature (T_M) and the blocking temperature (T_B) [67]. Between T_B and T_N (T_B<T_N), the intraparticle atomic moments lock together cooperatively and order antiferromagnetically under the influence of exchange interaction and the system responds reversibly or superparamagnetically to changes in the applied field within the time scale of the measurements for the disordered individual NP moments. In DC magnetization (zero-field cooled; ZFC) measurements, there is always a maximum at T_B. The Morin temperature decreases as the particle size decreases, tending to

disappear for particles smaller than about 8–20 nm [68, 69]. Crystal defects, strains, stoichiometric deviations and surface effects also tend to reduce the Morin temperature [63,70]. If the particles become small enough, the magnetic moment in a single domain fluctuates in direction due to thermal agitation, leading to superparamagnetic behavior above the blocking temperature T_B, and to spatial freezing of these moments below T_B.

1.6 Aim of the present work

As compared with bulk α-Fe_2O_3, the nanosized α-Fe_2O_3 is initiating its novel utilizations in various areas due to its new properties induced by its small size. The magnetic properties of Iron oxide nanoparticle can further be improved by doping of some metal ion like Al, Zn, Co, Nd, Mn etc in α-Fe_2O_3.

Few of rare earth (lanthanide) elements are metals that are ferromagnetic, and like iron they can be magnetized, but their Curie temperatures are below room temperature, so in pure form their magnetism only appears at low temperatures. The advantage of the rare earth compounds over other magnets is that their crystalline structures have very high magnetic anisotropy. This means that a crystal of the material is easy to magnetize in one particular direction, but resists being magnetized in any other direction [71].

It is evident from above discussion that a substantial number of magnetic data is available on both undoped and doped α-Fe_2O_3 NPs systems. However, it appears that there is very few magnetic data on Fe_2O_3 NPs doped with lanthanides. And till now, no data is found for Neomydium (Nd) doped α-Fe_2O_3. Under the circumstances it was thought worthwhile to undertake magnetic investigations of Nd doped α-Fe_2O_3 systems to throw more light on the nature of magnetism of the said iron oxide NPs. With this end in view, α-Fe_2O_3 NPs doped with different concentrations of Nd were prepared and subjected to further investigations.

The present works involves the preparation, characterization and study the nanocrystalline samples of $Fe_{2-x}Nd_xO_3$ (NFO) where x= 0.0, 0.1, 0.3 and 0.5 respectively. Our emphasis will be on Neutron diffraction studies since it is a direct tool to probe the ordering of the spins from unpaired electrons in material with magnetic properties.

REFRENCES

1. M I Baraton, *Synthesis, Functionalization, and Surface Treatment of Nanoparticles* (LosAngeles, CA: Am. Sci. Publ.) (2002)
2. R Rosensweig, *Ferrohydrodynamics* (Cambridge: Cambridge University Press)(1985)
3. S P Gubin, Yu A Koksharov Neorg. Mater. 38 1287 (2002)
4. Patil KC, Hegde MS, Tanu Rattan, Aruna ST. *Chemistry of nanocrystalline oxide materials: combustion synthesis, properties and applications (*Singapore: World Scientific) (2008).336
5. Merzhanov AG, Mukasyan AS. *Combustion of solid flame* (Moscow: Torus Press); (2007).
6. Mukasyan AS, Martirosyan K, editors. *Combustion of heterogeneous systems: fundamentals and applications for material synthesis* (Kerala, India: Transworld Research Network) (2007). 234.
7. Borisov AA, De Luca L, Merzhanov editors. AG, *Self-propagating high temperature synthesis of materials* (New York: Taylor and Francis) (2002) 337.
8. Segadaes AM. Eur Ceram News Lett 9 (2006) 1–5.
9. Varma A, Diakov V, Shafirovich E.; AIChE Journal 51 (2005) 2876–84.
10. Patil KC, Aruna ST, Mimani T.; Curr Opin Solid State Mater Sci 6 (2002) 507–12.
11. Merzhanov AG, Borovinskaya IP, Sytchev AE. SHS of nano-powders. In: Baumard J-F, editor. *Lessons in nanotechnology from traditional materials to advanced ceramics* (Dijon, France: Techna Group Srl) (2005) p. 1–27.
12. Mukasyan AS, Rogachev AS; Prog Energ Comb Sci 34 (2008) 377–416.
13. Filimonov IA, Kidin NI; Comb Explos Shock Waves 41 (2005) 639–56.
14. A. H. Morrish, *The physical Principles of Magnetism*, Wiley, New York, (1965)
15. S. Sun, *Adv. Mater.*, 18(2006) 393.
16. N´eel L, *Ann. Geophys,*. 5(1949) 99–136.
17. Brown W F Jr 1963 Thermal fluctuations of a single-domainparticle *Phys. Rev.* 130 1677–86
18. L.C. Sanchez, J.D. Arboleda, C. Saragovi, R.D. Zysler, C.A. Barrero, Physica B 389 (2007) 145–149.
19. Lili Li, Ying Chu, Yang Liu, Nanotechnology 18 (2007) 1–6.
20. P.G. Berkoff, H.R. Bertorello, M.I. Oliva, Physica B 398 (2007) 204–207.
21. C. Frandsen, C.R.H. Bahl, B. Lebech, K. Lefmann, L. Theil Kuhn, L. Keller, N.H.

Andersen, M.V. Zimmermann, E. Johnson, S.N. Klausen, S. Morup, Phys. Rev. B 72 (2005).

22. Z.H. Jing, S.H. Wu, Mater. Chem. Phys. 92 (2005) 600–603.
23. Marin Tadic, Dragana Markovic, Yojislav Spasojevic, Vladan Kusigerski, Maja Remskar, Janez Pirnat, Zvonko Jaglicic, J. Alloys Compd. 441 (2007) 291–296.
24. J.D. Uribe, J. Osorio, C.A. Barrero, D. Girata, A.L. Morales, A. Hoffmann, Microelectron. J. 39 (2008) 1391–1393.
25. Marin Tadic, Vladan Kusigerski, Dragana Markovic, Irena Milosevic, Vojislav Spasojevic, J. Magn. Magn. Mater. 321 (2009) 12–16.
26. John B. Parise, Darren R. Locke, Christopher A. Tulk, Ian Swainson, Lachlan Cranswick, Physica B 385-386 (2006) 391–393.
27. Jen-Ben Shi, Chia Wei Lee, Jhe-Wie Guo, Min-Jung Cheng, Chein Wu, Chih- Jung Chen, Yu-cheng Chen, Ya-Ting Lin, Chung-Chieh Chang, Mater. Lett. 61 (2007) 5268–5270.
28. N. Pailhe, A. Wattiaux, M. Gaudon, A. Demourgues, J. Solid State Chem. 181 (2008) 1040–1047. [15] Subarna Mitra, Soumen Das, Kalyan Mandal, Subhadra Chaudhuri, Nano- technology 18 (2007) 1–9.
29. R.M. Cornell, U. Schwermann, The Iron Oxides: Structure, Properties, Reactions, Occurrences and Uses, VCH, Weinheim, Germany, 1996.
30. D.J. Dunlop, Science 169 (1970) 858–860.
31. Subarna Mitra, Soumen Das, Kalyan Mandal, Subhadra Chaudhuri, Nano- technology 18 (2007) 1–9.
32. C.G. Shull, W.A. Strauser, E.O. Wollan, Phys. Rev. 83 (1951) 333–345.
33. I.E. Dzyaloshinskii, J. Phys. Chem. Solids 4 (1958) 241–255.
34. T. Moriya, Phys. Rev. 120 (1960) 91–98.
35. Dormann J L, Tronc E and Fiorani D 1997 Advances in Chemical Physics vol 98 (New York: Wiley) pp 283–494
36. Dormann J L and Fiorani D (ed) 1992 Magnetic Properties of Fine Particles (Amsterdam: North-Holland)
37. Zysler R D, VasquezMansilla M and Fiorani D 2004 *Eur. Phys.J.* B 41 171
38. Xu X N, Wolfus Y, Shaulov A, Yeshurun Y, Felner I, Norwik I,Koltypin Yu and Gedanken A 2002 *J. Appl. Phys.* 91 4611
39. Goya G F, Veith M, Rapalavicuite R, Shen H and Mathur S 2005 *Appl. Phys.* A 80 1523
40. Uhm Y R, Kim W W, Kim S J, Kim C S and Rhee C K 2003 *J. Appl. Phys.* 93 7196

41. Jiao F, Harrison A, Jumas J-C, Chadwick A V, Kockelmann W and Bruce P G 2006 *J. Am. Chem. Soc.*128 5468
42. Vasquez-Mansilla M, Zysler R D, Arciprete C, Dimitrijewits M I, Saragovi C and Greneche J M 1999 *J. Magn. Magn. Mater.* 204 29
43. Cannas C, Concas G, Gatteschi D, Falqui A, Musinu A, Piccaluga G, Sangregorio C and Spano G 2001 *Phys. Chem. Chem. Phys.* 3 832
44. Dormann J L, Fiorani D, Cherkaoui R, Spinu L, Lucar F, D'Orazio F, Nogub M, Tronc E, Jolivet J P and Garcia A 1999 *Nanostruct. Mater.* 12 757
45. Parker F T, Foster M W, Margulies D T and Berkowitz A E 1993 *Phys. Rev.* B 47 7885
46. Zysler R D, Fiorani D, Testa A M, Suber L, Agostinelli E and Godinho M 2003 *Phys. Rev.* B 68 212408
47. Fiorani D, Testa A M, Suber L, Angiolini M, Montone A and Polichetti M 1999 *Nanostruct. Mater.* 12 939
48. Carbone C, Benedetto F Di, Marescotti P, Sangregorio C, Sorace L, Lima N, Romanelli M, Lucchetti G and Cipriani C 2005 *Miner. Petrol.* 85 19
49. Mart´ınez B, Obradors X, Balcells Ll, Rouanet A and Monty C 1998 *Phys. Rev. Lett.* 80 181
50. Dimitrov D V, Hadjipanayis G C, Papaefthymiou V and Simopoulos A 1998 *J. Magn. Magn. Mater.* 188 8
51. Predoi D, Kuncser V, Filoti G and Schinteie G 2003 *J. Optoelectron. Adv. Mater.* 5 211
52. Klausen S N, Lefmann K, Lindg°ard P-A, Theil Kuhn L and Bahl C R H 2004 *Phys. Rev.* B 70 214411
53. P. Dutta, A. Manivannan, M.S. Seehra, Phys. Rev. B 70 (2004) 174428-1.
54. C. Caizer, I. Hrianca, Eur. Phys. J. B 31 (2003) 391.
55. R.D. Zysler, M. Vasquez Mansilla, D. Fiorani, Eur. Phys. J. B 41 (2004) 171.
56. R.D. Zysler, D. Fiorani, A.M. Testa, J. Magn. Magn. Mater. 224 (2001) 5.
57. Y.Y. Xu, X.F. Rui, Y.Y. Fu, H. Zhang, Chem. Phys. Lett. 410 (2005) 36.
58. A.M. Testa, S. Foglia, L. Suber, D. Fiorani, L. Casas, R. Roig, E. Molins, J.M. Grene`che, J. Tejada, J. Appl. Phys. 90 (2001) 1534.
59. F. Hong, B.L. Yang, L.H. Schwartz, H.H. Kung, J. Phys. Chem. 88 (1984) 2525.
60. F. Bondioli, A.M. Ferrari, C. Leonelli, T. Manfredini, Mater. Res. Bull. 32 (1998) 723.
61. R.L. Blake, R.E. Hessevick, T. Zoltai, L.W. Finger, Am. Miner. 51 (1966) 123.
62. A. Oles´, F. Kajzar, M. Kucab, W. Sikora, Magnetic Structures Determined by Neutron Diffraction, Pan´stwowe Wydawnictwo Naukowe, Warszawa-Krako´w, 1976, p. 372.

63. F.J. Morin, Phys. Rev. 78 (1950) 819.
64. C. Guilland, J. Phys. Radium 12 (1951) 489.
65. J.O. Artman, J.C. Murphy, S. Foner, Phys. Rev. 138 (1965) A912.
66. C.G. Shull, W.A. Strauser, E.O. Wollan, Phys. Rev. 83 (1951) 333.
67. R.D. Zysler, M. Vasquez, C. Arciprete, M. Dimitrijewits, D. Rodriguez-Sierra, C. Saragovi, J. Magn. Magn. Mater. 224 (2001) 39.
68. N. Amin, S. Arajs, Phys. Rev. B 35 (1987) 4810.
69. R. Nininger Jr., D. Scrhroeer, J. Phys. Chem. Solids 39 (1978) 187.
70. M.Z. Dang, D.G. Rancourt, J.E. Dutrizac, G. Lamarche, R. Provencher, Hyperfine Interact.117 (1998) 271.
71. Cullity, B.D.; C.D. Graham (2008). *Introduction to Magnetic Materials*. Wiley-IEEE. ISBN 0471477419.

Chapter 2

Materials and Methods

2.1 Synthesis of $Nd_xFe_{2-x}O_3$ nanoparticles by combustion method

In the last decade, the chemical methods of preparation of nanoparticles have been used for the fabrication of several types of nanoparticles where control on the size, composition, etc., could have been achieved. Iron oxide nanoparticles have been prepared by variety of methods including sonochemical, mechanochemical synthesis, hydrolysis and thermolysis of precursors, polymeric matrices, coprecipitaion and combustion method etc.

Combustion synthesis (CS) method or self-propagating high-temperature synthesis (SHS) is an effective, low-cost method for production of various industrially useful materials. Today CS has become very popular approach for synthesis of nanomaterials [1-6]. It is a versatile, simple and rapid process, which allows effective synthesis of a variety of nanosize materials. This process involves a self-sustained reaction in homogeneous solution of different oxidizers (e.g., metal nitrates) and fuels (e.g., urea, glycine, hydrazides). Depending on the type of the precursors, as well as on conditions used for the process organization, the CS may occur as either volume or layer-by-layer propagating combustion modes. This process not only yields nanosize oxide materials but also allows uniform (homogeneous) doping of trace amounts of rare-earth impurity ions in a single step.

The chemical reaction occurring in the combustion process can be written as:

$M(NO_3)_3(aq) + Fe(NO_3)_3\ (aq) + C_2H_5NO_2\ (aq) \rightarrow M_xFe_{2-x}O_3\ (s) + CO_2\ (g) + H_2O\ (g) + N_2(g)$.

Where, M is the metal nitrate to be doped in iron oxide.

Fuel possesses a high heat of combustion. It is an organic fuel and provides a platform for redox reactions during the course of combustion. But In our study, the desired nanoparticles were synthesized without using any kind fuel and simply precursor metal nitrates were used.

2.2 Experimental

Nanocrystalline (powdered) samples of $Nd_xFe_{2-x}O_3$ (NFO) series were prepared by combustion method, where x=0.0, 0.1, 0.3 and 0.5 respectively. The precursor used for the synthesis of nanocrystalline sample of NFO series were **(i) iron nitrate nonahydrate, Fe $(NO_3)_3.9H_2O$; and (ii) Neodymium nitrate nonahydrate, $Nd(NO_3)_3.9H_2O$**. Initially, Iron nitrate nonahydrate, $Fe(NO_3)_3.9H_2O$; and Neodymium nitrate nonahydrate, $Nd(NO_3)_3.9H_2O$ were taken in stochiometric ratios and ground to make it homogenous mixture. The powdered mixture of each sample of series was heat treated at 400° C for about 10 minutes. The cooled sample is homogenized again and further calcined for 2 hours at 400° C. Magnetic measurements were performed using SQUID magnetometer. For neutron diffraction (ND) measurements samples of NFO series were filled in vanadium can. Room temperature ND experiments were carried out on the Focusing Crystal diffractometer (FCD) at Dhruva reactor, BARC, India, using a wavelength of 1.48Å [7]. The nuclear and magnetic structures of the NFO compounds were refined by Rietveld method using FullProf program [8-10].

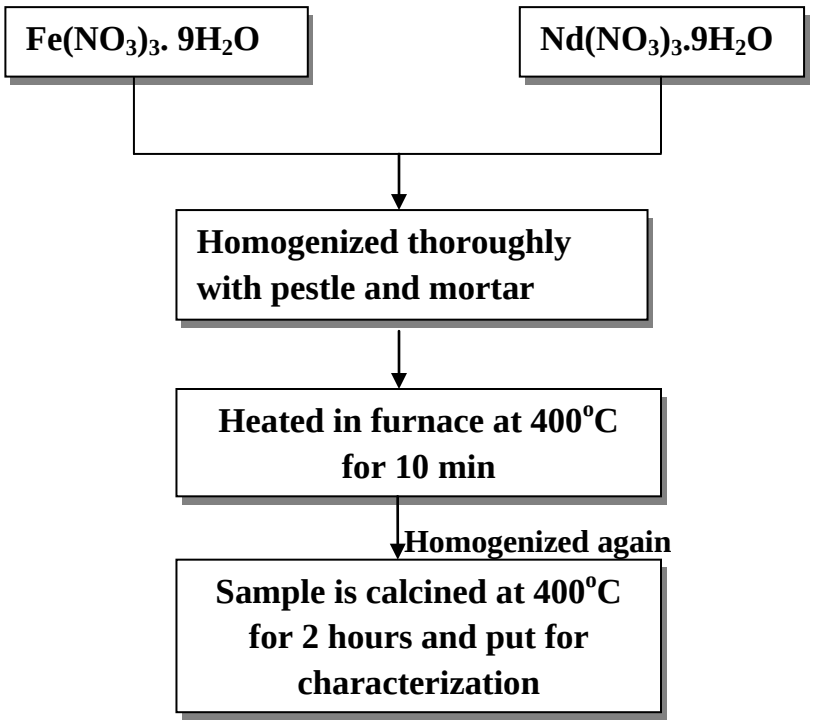

Fig 2.1: Flow Chart depicting experimental technique to synthesize $Nd_xFe_{2-x}O_3$ nanoparticle through combustion method without using any fuel.

2.3 Characterization Techniques

The characterization of the powder was carried out using following techniques to evaluate the size, crystallinity, morphology and magnetic nature of particles.

2.3.1 X-Ray Diffractometer (XRD)

X-ray powder diffraction (XRD) is a rapid analytical technique primarily used for phase identification of a crystalline material and can provide information on unit cell dimensions. The analyzed material is finely ground, homogenized, and average bulk composition is determined.

X-ray diffraction is based on constructive interference of monochromatic X-rays and a crystalline sample. These X-rays are generated by a cathode ray tube, filtered to produce monochromatic radiation, collimated to concentrate, and directed toward the sample. The interaction of the incident rays with the sample produces constructive interference (and a diffracted ray) when conditions satisfy Bragg's Law ($n\lambda=2d \sin\theta$). This law relates the wavelength of electromagnetic radiation to the diffraction angle and the lattice spacing in a crystalline sample. These diffracted X-rays are then detected, processed and counted. By scanning the sample through a range of 2θangles, all possible diffraction directions of the lattice should be attained due to the random orientation of the powdered material. Conversion of the diffraction peaks to d-spacings allows identification of the mineral because each mineral has a set of unique d-spacings.

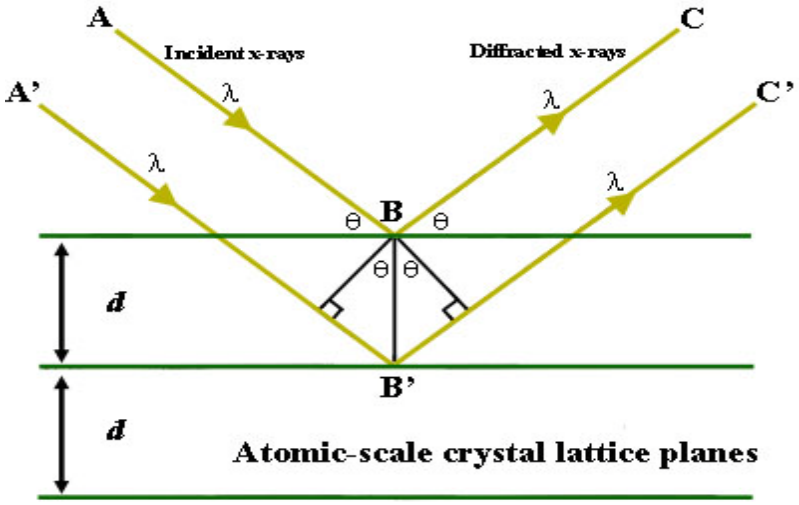

Fig 2.2: Bragg diffraction. Two beams with identical wavelength and phase approach a crystalline solid and are scattered of two different atoms within it. The lower beam traverses an extra length of 2dsinθ.

The crystallographic interpretations were performed by X-ray diffractometer (Bruker AXS D8 Advance X-ray Diffractometer) using Cu-Kα wavelength (λ=1.54059 Å) and scanning in the 2θ

range from 20^{o} to 80^{o}. Phase identification of the precipitated powders was performed by comparing X-ray Powder diffraction (XRD) data against the JCPDS standards database.

2.3.2 Scanning Electron microscopy

A **scanning electron microscope** (**SEM**) is a type of electron microscope that images a sample by scanning it with a high-energy beam of electrons in a raster scan pattern. The electrons interact with the atoms that make up the sample producing signals that contain information about the sample's surface topography, composition, and other properties such as electrical conductivity. The types of signals produced by an SEM include secondary electrons, back-scattered electrons (BSE), characteristic X-rays, light (cathodoluminescence), specimen current and transmitted electrons. Secondary electron detectors are common in all SEMs, but it is rare that a single machine would have detectors for all possible signals. The signals result from interactions of the electron beam with atoms at or near the surface of the sample. Due to the very narrow electron beam, SEM micrographs have a large depth of field yielding a characteristic three-dimensional appearance useful for understanding the surface structure of a sample. Back-scattered electrons (BSE) are beam electrons that are reflected from the sample by elastic scattering. BSE are often used in analytical SEM along with the spectra made from the characteristic X-rays. Because the intensity of the BSE signal is strongly related to the atomic number (Z) of the specimen, BSE images can provide information about the distribution of different elements in the sample.

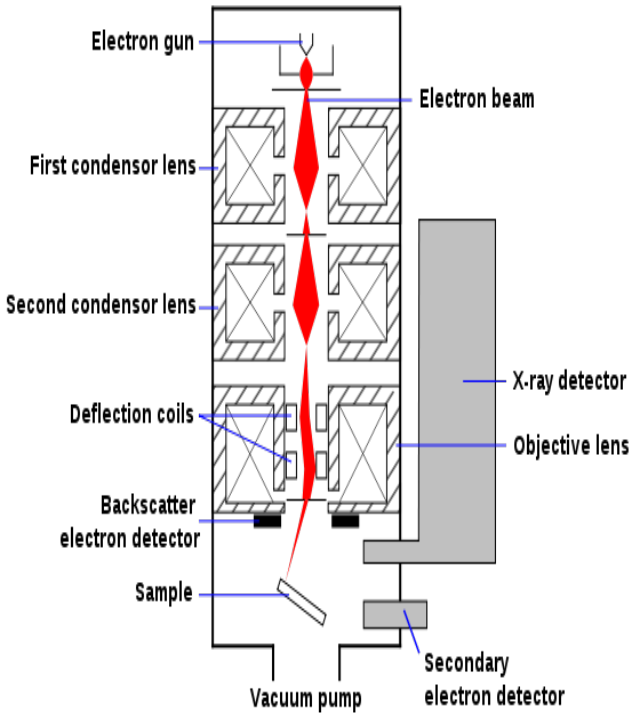

Figure 2.3: Schematic diagram of a SEM.

The topological features and surface morphologies were studied using a scanning electron microscope (SEM: ZEISS EVO MA-10) equipped with an energy dispersive spectrometer (EDS: Oxford Link ISIS 300).

2.3.3 Magnetic Characterisation

For the magnetic characterization of the sample, SQUID (Superconducting Quantum Interface Device) technique is used. The SQUID magnetometer is extremely low impedance, high sensitivity flux detector capable of operating over a wide range of frequencies [7]. The magnetometer detects the flux produced by a sample passing slowly through a pickup coil. The SQUID does not measure the field from the sample directly but is coupled inductively to superconducting pickup coils. Changes in flux set up a persistent current in the pickup coil in the SQUID transformer circuit. A feedback, which is generated to either null the persistent current in the superconducting circuit or change the flux in the SQUID, is proportional to the magnetic moment of the sample. The sample is moved slowly through the pickup coils. The superconducting shield shields the SQUID. This shield not only protects the SQUID from high stray magnetic fields from the superconducting magnet but also reduces ambient stray field interference.

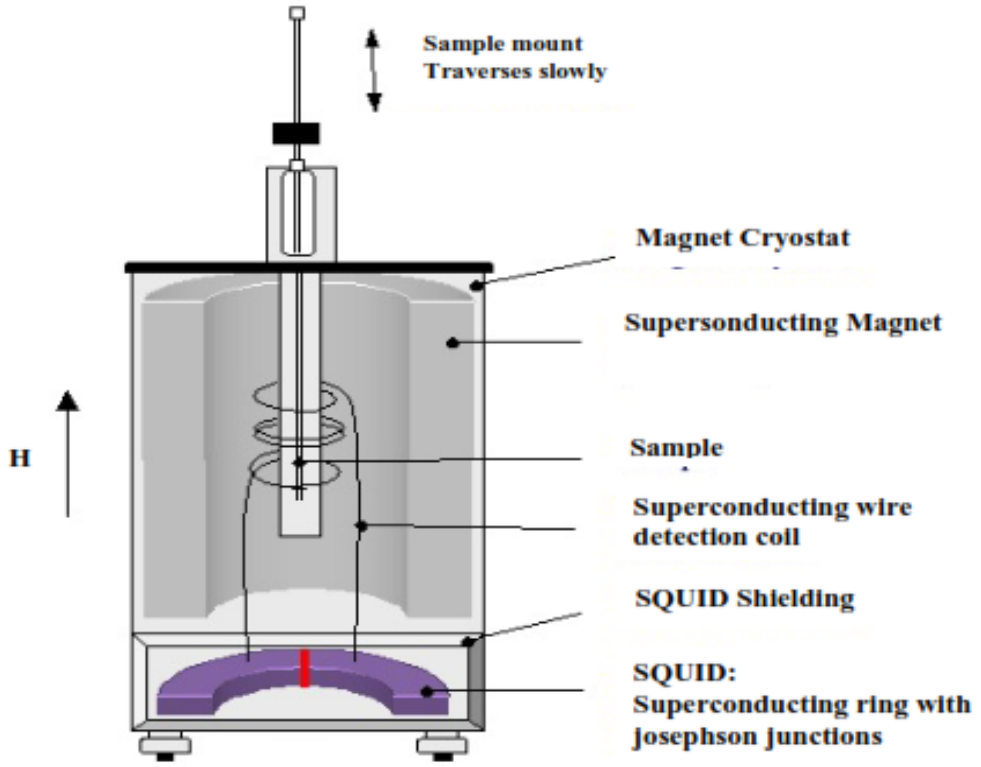

Fig. 2.4: Schematic diagram of SQUID.

2.3.4 Neutron Diffraction

Neutron diffraction or **elastic neutron scattering** is the application of neutron scattering to the determination of the atomic and/or magnetic structure of a material. The technique is similar to X-ray diffraction but due to the different scattering properties of neutrons versus x-rays complementary information can be obtained. Neutrons interact with matter differently than x-rays. X-rays interact primarily with the electron cloud surrounding each atom. The contribution to the diffracted x-ray intensity is therefore larger for atoms with a large atomic number (Z) than it is for atoms with a small Z. On the other hand, neutrons interact directly with the *nucleus* of the atom, and the contribution to the diffracted intensity is different for each isotope; for example, regular hydrogen and deuterium contribute differently. Many neutron sources are equipped with liquid helium cooling systems that allow to collect data at temperatures down to 4.2 K. The superb high angle (i.e. high *resolution*) information means that the data can give very precise values for the atomic positions in the structure.

Neutron Diffraction experiments were carried out at room temperature on the Focusing Crystal diffractometer (FCD) at Dhruva reactor, BARC, India, using a wavelength of 1.48Å [8]. The nuclear and magnetic structures of the NFO compounds were refined by Rietveld method using FullProf program [9-11].

2.3.5 Thermo-gravimetric Analysis

Thermo-gravimetric (TGA) is a type of testing performed on samples that determines changes in weight in relation to change in temperature [12]. Such analysis relies on a high degree of precision in three measurements: weight, temperature, and temperature change. TGA is commonly employed in research and testing to determine characteristics of materials such as polymers, to determine degradation temperatures, absorbed moisture content of materials, the level of inorganic and organic components in materials, decomposition points of explosives, and solvent residues. It is also often used to estimate the corrosion kinetics in high temperature oxidation.

Simultaneous TGA-DTA/DSC measures both heat flow and weight changes (TGA) in a material as a function of temperature or time in a controlled atmosphere. Simultaneous measurement of these two material properties not only improves productivity but also simplifies interpretation of the results.

For TGA experiments measurements, of the heat flow were recorded in the temperature range of 25-900^{o}C for a few milligrams of a sample placed in alumina pans and heated at a rate of 5^{o}C per min.

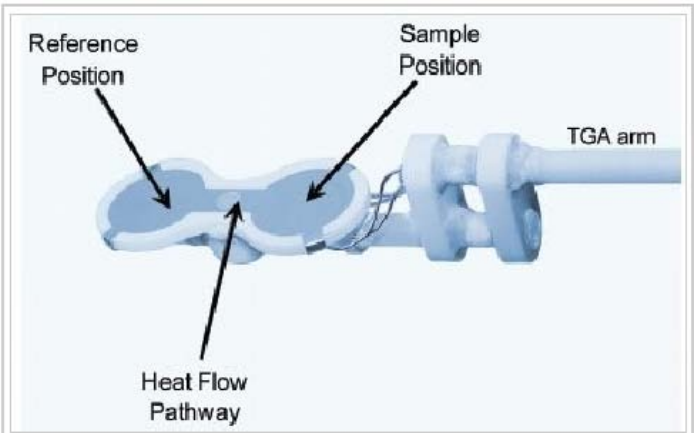

Figure 2.5: TGA/DSC two-thermocouple DSC sensor. The heat flow pathway of the sensor is fixed and can be calibrated to give accurate DSC heat flow response. The surface is made of platinum for high thermal conductivity, and supported by a ceramic holder.

REFRENCES

1. Segadaes AM. Oxide powder synthesis by the combustion route. Eur Ceram News Lett 2006; 9:1–5.
2. Varma A, Diakov V, Shafirovich E. Heterogeneous combustion: recent developments and new opportunities for chemical engineers. AIChE J 2005;51:2876–84.
3. Patil KC, Aruna ST, Mimani T. Combustion synthesis: an update. Curr Opin Solid State Mater Sci 2002;6:507–12.
4. Merzhanov AG, Borovinskaya IP, Sytchev AE. SHS of nano-powders. In: Baumard J-F, editor. Lessons in nanotechnology from traditional materials to advanced ceramics. Dijon, France: Techna Group Srl; 2005. p. 1–27.
5. Mukasyan AS, Rogachev AS. Discrete reaction waves: gasless combustion of solid powder mixtures. Prog Energ Comb Sci 2008;34:377–416.
6. Filimonov IA, Kidin NI. High-temperature combustion synthesis: generation of electromagnetic radiation and the effect of external electromagnetic fields. Comb Explos Shock Waves 2005;41:639–56.
7. D. Drung, C. Assmann, J. Beyer, A. Kirste, M. Peters, F. Ruede, and Th. Schurig (2007). "Highly sensitive and easy-to-use SQUID sensors". *IEEE Transactions on Applied Superconductivity* **17** (2): 699.
8. V. Siruguri, P. D. Babu, M. Gupta, A. V. Pimpale and P. S. Goyal, *Pramana - J. Phys.* **71** (2008) 1197.
9. T. Roisnel, J. Rodríguez-Carvajal, WINPLOTR, Laboratoire Léon Brillouin (CEA-CNR), Centre dÉtudes de Saclay, 91191 Gif-sur-Yvette, Cedes (France) and Laboratoire de Chimie du Solide et Inorganique Moléculaire (UMR6511), Université de Rennes 1, 35042 Rennex cedex (France). http://www-llb.cea.fr/fullweb/winplotr/winplotr.htm.
10. J. Rodriguez-Carvajal, *Physica B* **192** (1993) 55.
11. H. M. Rietveld, *J. Appl. Cryst.* **2** (1969) 65.
12. Mansfield, E.; Kar, A.; Quinn, T. P.; Hooker, S. A. (2010). "Quartz Crystal Microbalances for Microscale Thermogravimetric Analysis". *Analytical Chemistry* **82** (24): 101116152615035.

Chapter 3

Results and Discussion

3.1. X-Ray Diffraction

Preliminary structural characterizations of all the four samples studied in $Fe_{2-x}Nd_xO_3$ (NFO) series were carried out by analyzing the room temperature powder x-ray diffraction patterns. XRD patterns as shown in Fig. 3.1(a) clearly indicate that the compounds of this series forms in the hematite (α-Fe_2O_3) structure. All the four compounds exhibited rhombohedral symmetry having space group R-3c with hexagonal setting and the patterns were indexed on the basis of α-Fe_2O_3 structure. The refined unit cell parameters for the x = 0.0 sample were in good agreement with the reported values [1]. A non-systematic variation in lattice constants has been observed with increasing Nd content in these samples, which may be due to various effects taking place in this series. Firstly, it is difficult to predict which site of Fe does Nd replaces, as there is non-linear variation in both ab-plane as well as c-axis (*a*, and *c* values of the unit cell). The variation of the cell constants due to Nd substitution is shown in Fig. 3.2. We also tried to synthesize the sample having x= 0.7 but the formation of some impurity phases start to appear when 'x' exceeds to 0.5 as shown in Fig. 3.1(b). Hence our study is limited to x= 0.5 for further studies.

Table 3.1 shows various parameters obtained from the XRD. It was shown that the rhombohedral lattice of iron oxide has slight increase in 'a', 'c' and 'V' lattice parameters upon Nd substitution.

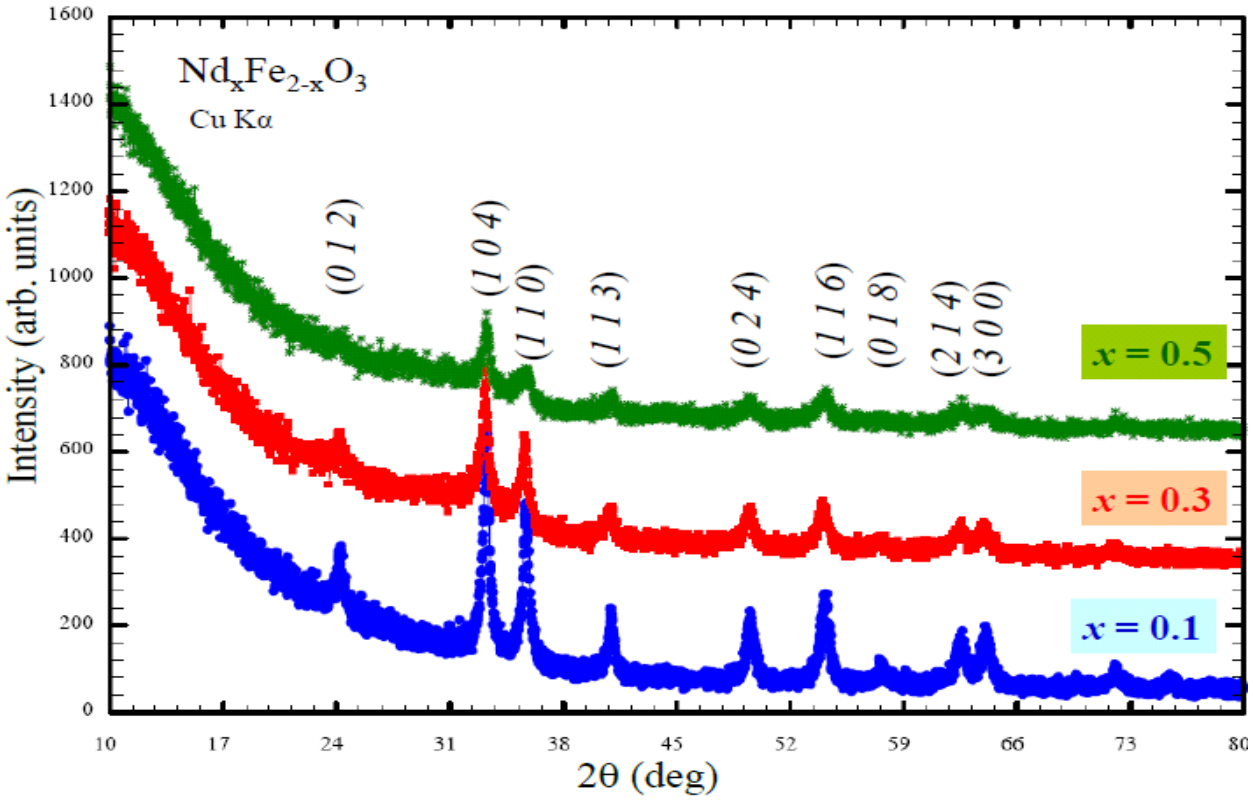

Fig. 3.1 (a): XRD of $Fe_{2-x}Nd_xO_3$ sample, where x=0.1, 0.3 and 0.5 respectively.

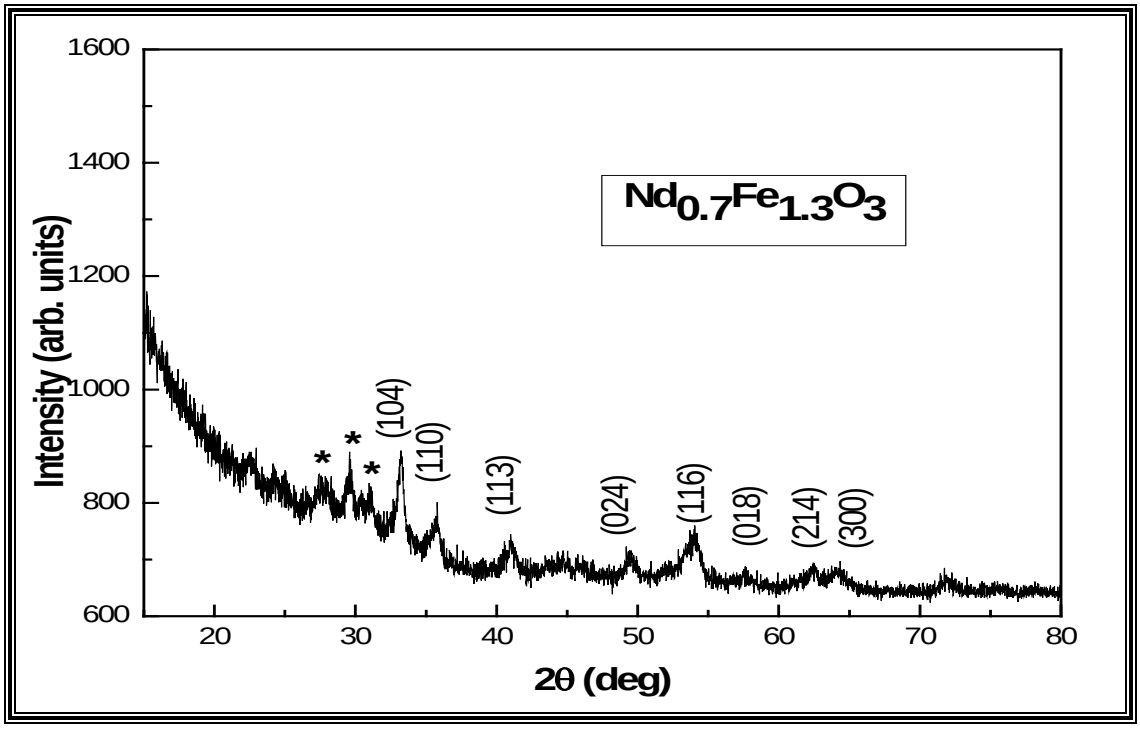

Fig. 3.1 (b): XRD of $Fe_{1.3}Nd_{0.7}O_3$ sample (***** marks shows the few extra peaks of the second phase)

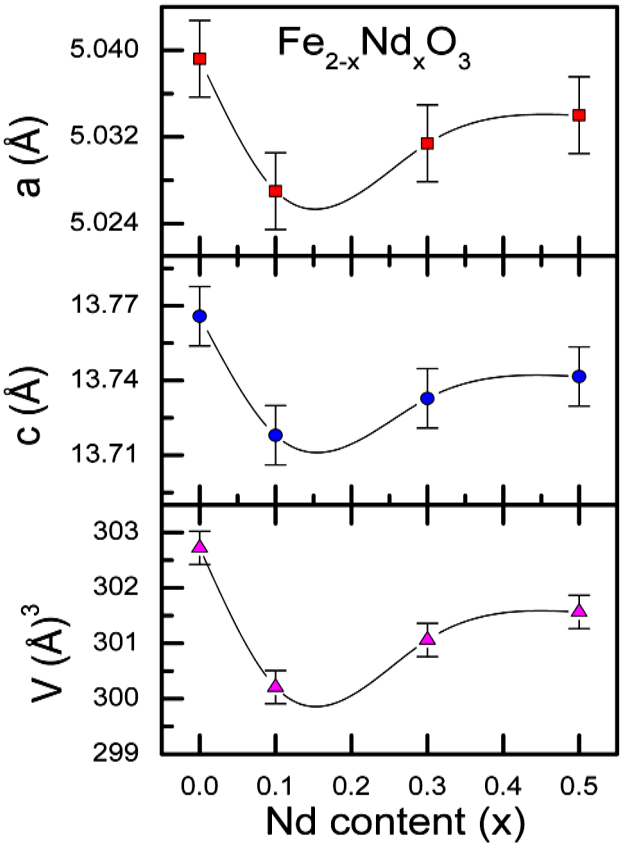

Fig. 3.2: The values of lattice constants for $Fe_{2-x}Nd_xO_3$ samples are shown as a function of the dopant (Nd) concentration. Non-systematic variation in lattice constants has been observed with increasing Nd.

X	2θ	hkl	FWHM	d-spacing	a	c	V
0.1	33.229	104	0.45408	2.6940	5.0270	13.718	300.209
	35.692	110	0.3866	2.5135			
0.3	33.195	104	0.5870	2.6967	5.0314	13.732	301.060
	35.66	110	0.4244	2.5157			
0.5	33.174	104	0.68195	2.6983	5.0340	13.741	301.565
	35.66	110	0.4272	2.5170			

Table 3.1:- Various lattice parameters obtained from the XRD.

3.2. Scanning Electron Microscope (SEM)

To visualize the images of the particles of the prepared material, SEM has been performed. SEM images demonstrate that the particles have wide size distribution. Large agglomeration of the nanoparticles is clearly observed. In fact Fe_2O_3 is very well known for the formation of agglomerated nanoparticles because of their magnetic nature [4]. To get the better idea of the exact sizes of the particles Transmission electron microscopy (TEM) is preferred.]

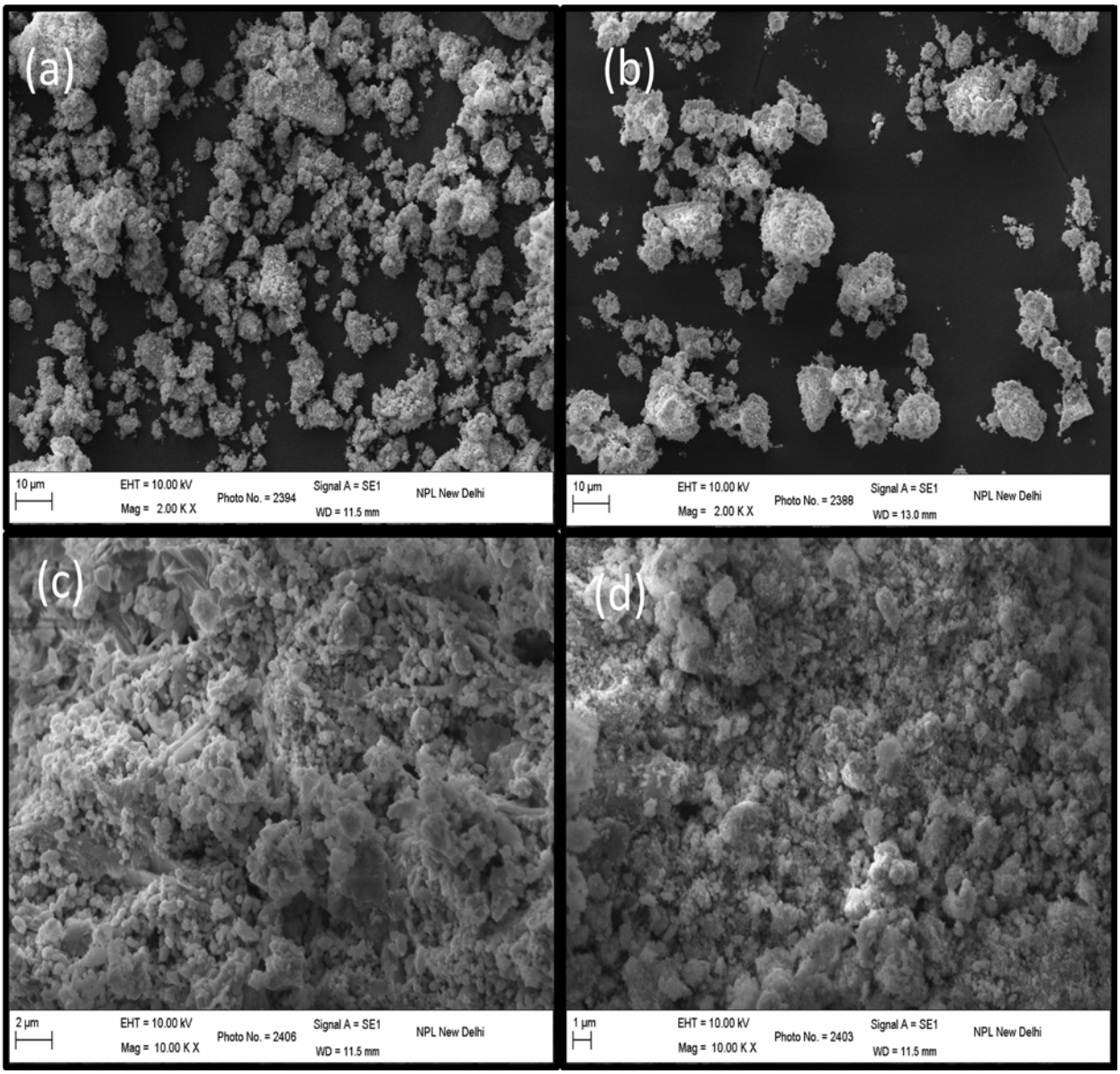

Fig. 3.3: SEM micrograph of the prepared NFO series (a) $Nd_{0.1}Fe_{1.9}O_3$ (b) $Nd_{0.3}Fe_{1.7}O_3$ (c) $Nd_{0.5}Fe_{1.5}O_3$ and (d) $Nd_{0.7}Fe_{1.3}O_3$.

3.3. Magnetization Measurements

Magnetization as a function of applied field was performed at room temperature for all the samples of the NFO series. Interestingly, no saturation of moments is observed in any of the samples up to field strengths of 60 kOe. The non-saturation of the magnetization is a clear indication of the presence of superparamagnetic particles at room temperature. Here again the non-saturation of the curves agrees with the average particle size, i.e. smaller the size of the particles larger is the non-saturation field. However, observation of a very small hysteresis along with the non saturation of the curves for all the samples reveals wide particle size distribution. Such an observation exhibits that the samples consists not only superparamagnetic particles but also have agglomerated particles that contribute to the hysteresis behavior. Both, coercivity (H_c) and remnant magnetization (M_r) were observed and the values are tabulated in the Table 3.2. We see that the sample with larger average size or larger agglomerates has large value of H_c compared to the samples with smaller average size particle. This variation of H_c with size has already been explained by Cullity [2]. Also the explanation for such behavior was given by Rath *et. al* [3] where they explain that coercivity increases for the agglomerated particles since they experience the external field as well as the stray fields of neighboring particles.

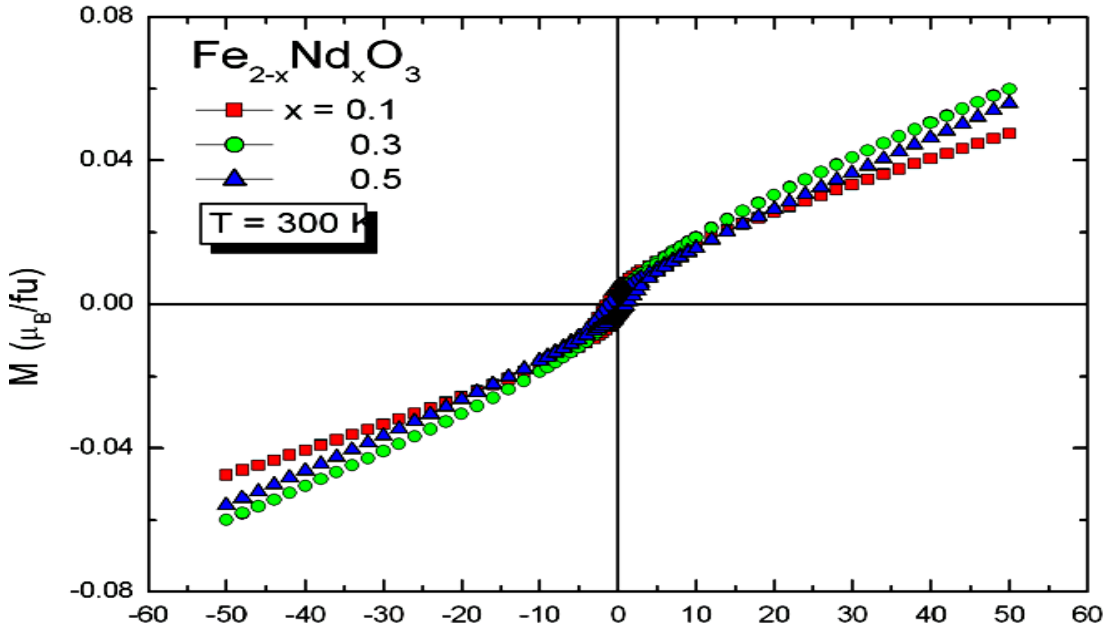

Fig 3.4:- Magnetization (M) as a function of varying field (H) for $Nd_xFe_{2-x}O_3$ sample. The M(H) curves were recorded at room temperature.

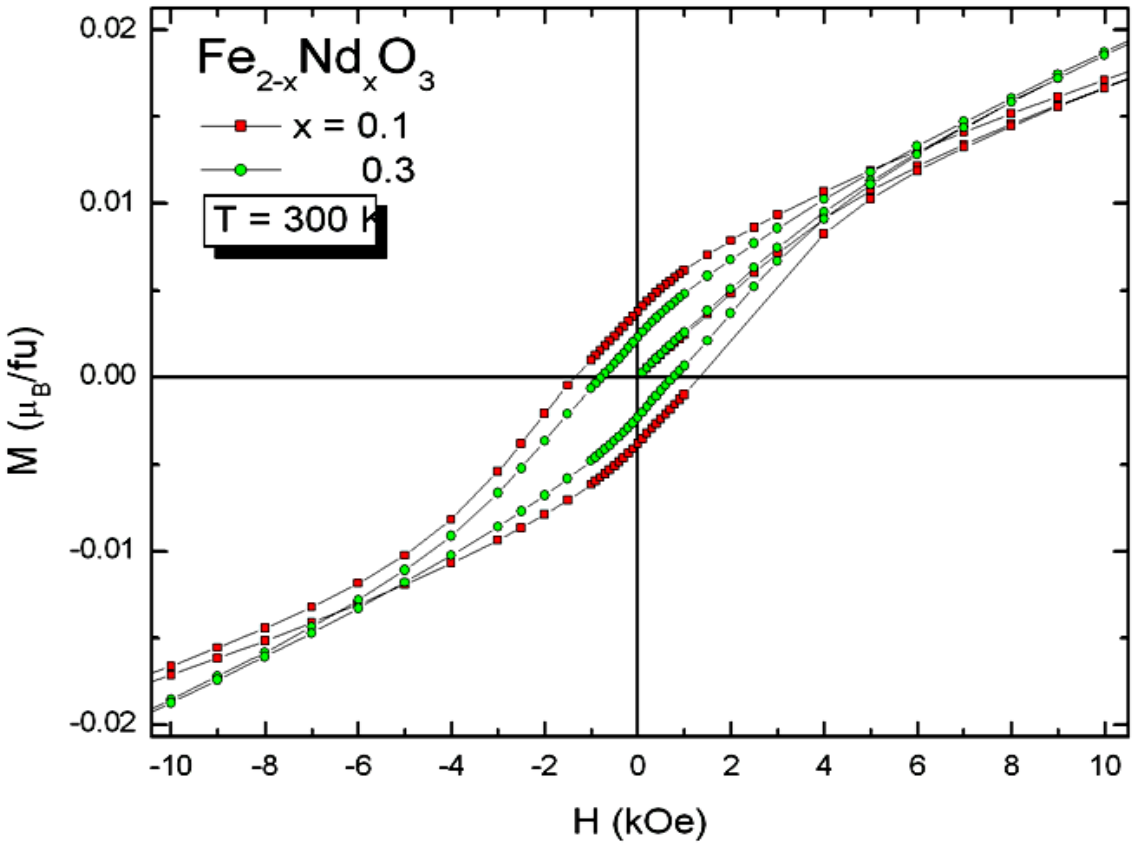

Fig. 3.5:- The M(H) curves around the origin of the hysteresis loop are shown on an expanded scale. The M(H) curves for all the samples exhibits coercivity and remnant magnetization.

X	$-H_{c1}$	H_{c2}	M_r	$-M_r$	Average Particle size (nm)	T_B(K)	θ_p (K)	Upturn temp (K)
0.1	1.325	1.327	0.00375	0.00374	31	161	185	18
0.3	0.741	0.784	0.00227	0.00228	15	100	152	21
0.5	1.186	1.206	0.00258	0.00260	16	78	142	40

Table 3.2: Coericivity (H_c), Remenance field (M_r), Blocking temperature (T_B), θ_p and upturn temperature derived from magnetic measurements of $Fe_{2-x}Nd_xO_3$ at 300 K. Average particle size derived from neutron data.

The Zero Field Cooled (ZFC) magnetization curve, $\chi(T)$ was measured in a field of 100 Oe and temperature range of 0-300K as shown in Fig. 3.6. The pristine sample α-Fe_2O_3 is well known in the literature. In Fig. 3.6, we have shown $\chi(T)$ plot for Nd doped Fe_2O_3. The figure clearly shows the change in the magnetic behavior with increasing Nd concentration. The $\chi(T)$ exhibits a broad cusp that can be correlated to the wide particle size distribution in the samples. And the maxima of the cusp in the $\chi(T)$ curve correspond to the blocking temperature (T_B) of the respective sample. It is very well known that above T_B the particles in the material are superparamagnetic and below T_B the moments are frozen in random field direction [4, 5]. T_B values are also tabulated in Table 3.2. The blocking temperature decreases with increasing Nd concentration which signifies the dilution of magnetism. At very low temperature in the $\chi(T)$ curve an upturn is observed, the values for that has been tabulated in the table 3.2. Such an upturn can be attributed to various reasons, such as (i) initiation of Nd ordering at low temperatures, (ii) Since the system has particles with wide range of sizes, so existing particles in SPM state will undergo *'blocking'* at different temperatures. Therefore, we believe that at such low temperatures also fraction of particles exist whose magnetic moment is not blocked [5] (iii) Occurrence of spin glass state that can be characterized by random, yet cooperative spins, that can lead to a metastable state without usual magnetic long range ordering [6].

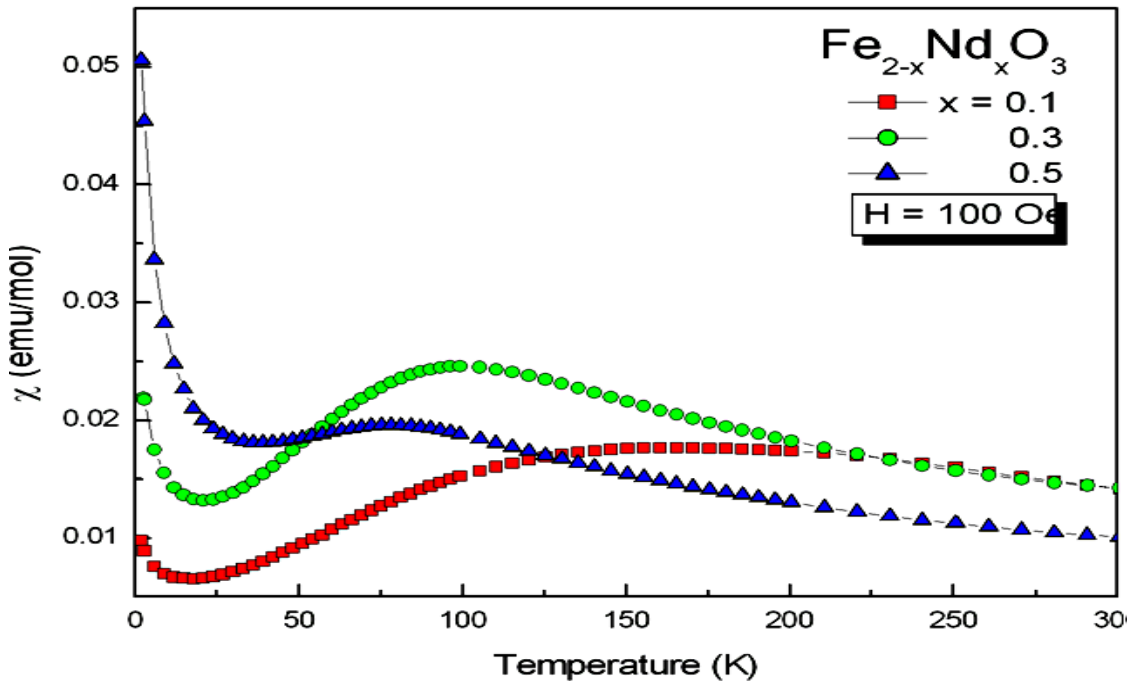

Fig. 3.6:- $\chi(T)$ for $Fe_{2-x}Nd_xO_3$ samples measured in a field of 100 Oe.

The figure 3.7 also shows the inverse magnetic susceptibility plotted as a function of temperature. From the linear region of the χ^{-1} vs. T plot, the paramagnetic Curie temperature (θ_p) could be calculated using the Curie-Weiss law: $\chi = C/(T-\theta_p)$. The effective Bohr magneton number, μ_{eff} has also been calculated using the Curie constant (C). With increasing Nd content, θ_p decreases from -185 K to -142 K. Similarly, the μ_{eff} also decreases. The negative sign of θ_p indicates predominant antiferromagnetic interactions. The figure also clearly shows the change in the magnetic behavior with increasing Nd concentration.

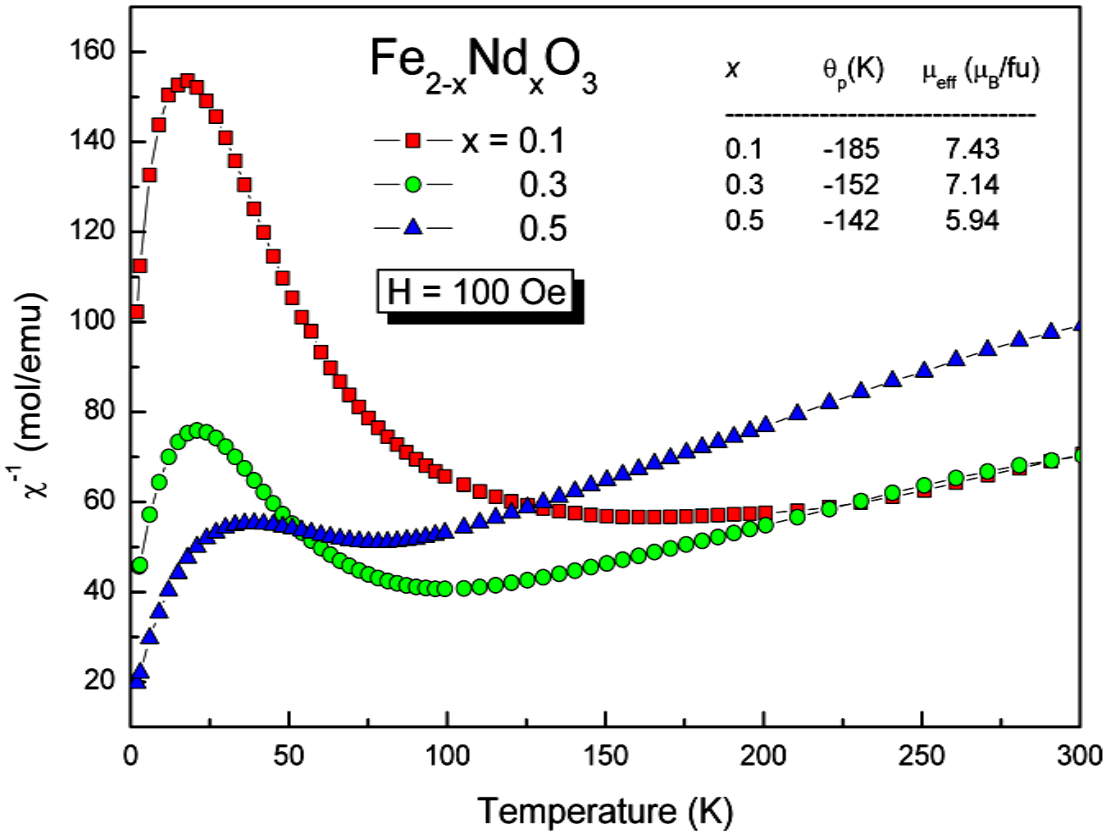

Fig. 3.7:- The inverse magnetic susceptibility is plotted as a function of temperature. The values of paramagnetic Curie temperature (θ_p) and effective Bohr magneton number (μ_{eff}).

3.4. Neutron Diffraction (ND) Measurements

Neutron diffraction (ND) is a powerful technique for understanding both crystal and magnetic structure and hence a direct correspondence between the structure and magnetism can be drawn. As seen from magnetization measurements, the compounds of $Fe_{2-x}Nd_xO_3$ (NFO) series exhibits magnetism at room temperature, hence for better understanding of the crystal and magnetic structure, room temperature ND experiments were carried out on powdered samples of NFO series.

Since the samples were magnetic at room temperature, as discussed above, Bragg peaks owing to magnetic ordering could be expected at room temperature itself. The advantage of ND over XRD is that precise cation distribution can be achieved. Hence, using the lattice constants observed from XRD refinement, and using the same structural model, the ND patterns of the NFO series of compounds were analyzed. The results of refinement are tabulated in Table 3.3. The particle size could also be calculated from the refinement of the powder diffraction data. The refinement of ND patterns, shown in Fig. 3.9 confirms that the compound forms into Al_2O_3 type rhombohedral structure with hexagonal setting structure space group, *R*-3*c* (International Table of Crystallographic Data, Symmetry number 167: H). The structure is characterized by a large *c/a* ratio of about 2.73 and has 6 cells per formula unit (Z = 6). The magnetic and crystal structure of the hematite (α-Fe_2O_3) is reported in literature [1]. Fe occupies the 12*c* and O is at 18*e* crystallographic sites in Wyckoff's notations in the space group *R*-3*c*.

In Fig. 3.8, ND patterns for all the four compounds is shown along with the Rietveld refinement for x = 0.0 sample. The whole pattern could be refined assuming a nuclear (crystal) and a magnetic structure. For magnetic structure, 12 sites for Fe atoms obtained from the symmetry operators were considered with the space group *R*-1 (lowest symmetry space group to generate all possible magnetic positions) and added as a second phase, for refinement along with the nuclear structure. A propagation vector, k = (0 0 0) was taken for magnetic cell refinement, which means that the magnetic cell and crystallographic cell dimensions are same. Refinement for all the patterns converged with reasonable refinement values. The results of nuclear and magnetic structure refinement for all samples are compiled in Table 3.3.

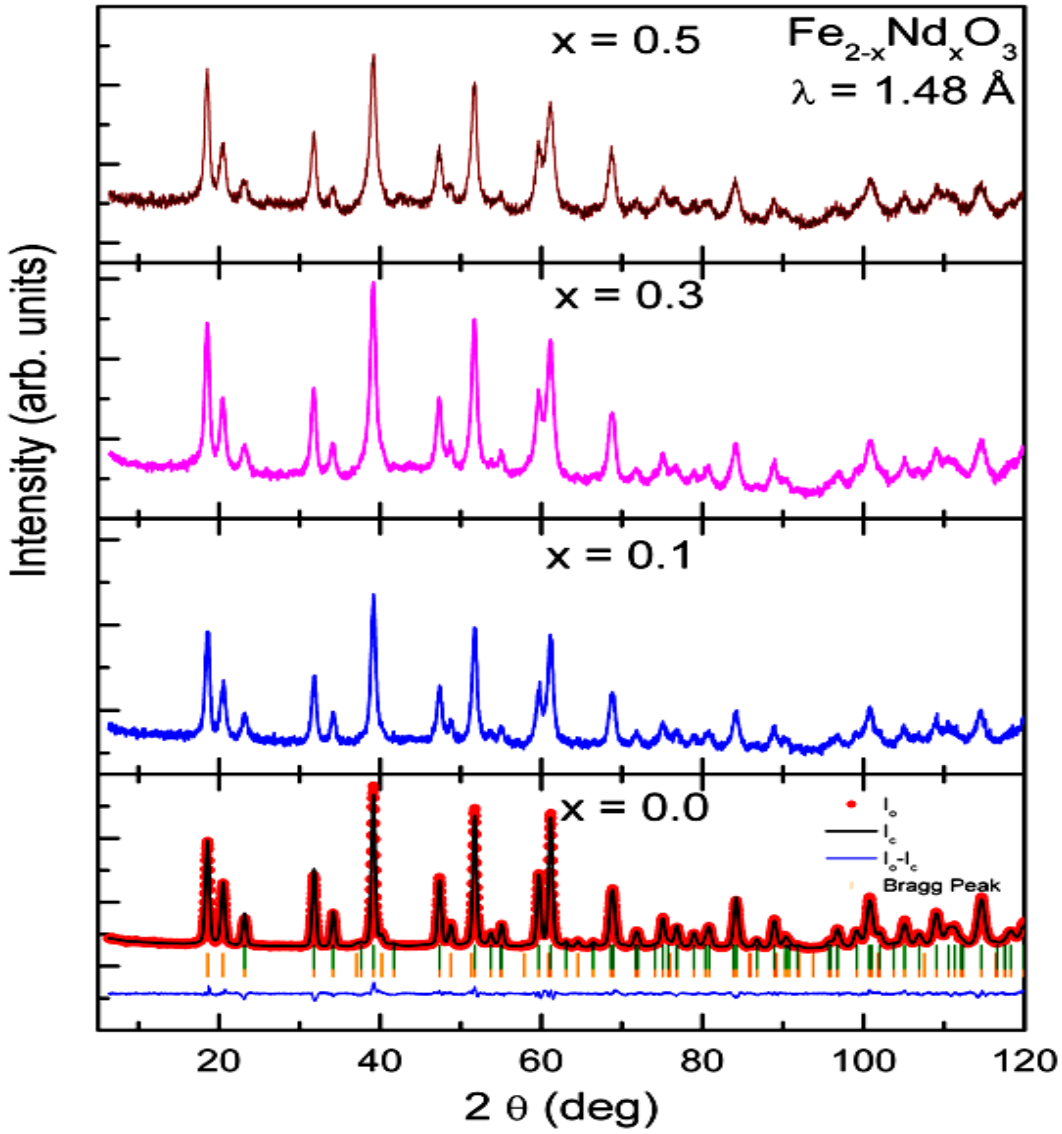

Fig. 3.8:- Neutron diffraction patterns of powder samples of $Fe_{2-x}Nd_xO_3$ series measured at room temperature. Rietveld refinement for x = 0.0 sample has been shown. The red filled data points represent the original data; black line passing through the data points indicates the calculated profile. The difference between the observed and calculated patterns is shown by the continuous blue line. The colored vertical tick marks represents nuclear Bragg (green) and magnetic Bragg (orange) peaks respectively.

The crystal structure for Nd doped Fe_2O_3 is shown in Fig. 3.9. The shortest and longest distance between Fe-O is 1.949 Å and 2.110 Å respectively. The unequal bond lengths describe the distortions in the polyhedra around Fe atom. We have also calculated the bond valence sums (BVS) using Fullprof, while refining the pattern. It is interesting to note that with increasing Nd content the BVS of Fe(Nd) and O increases, which means that Nd-substitution strengths the bonding between Fe and O.

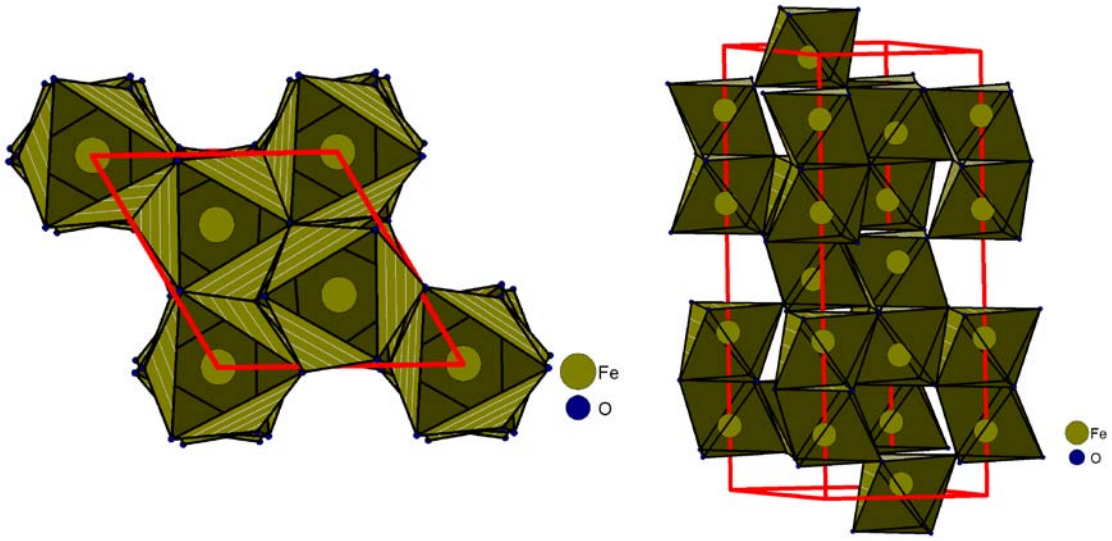

Fig. 3.9: The crystal structure of $Fe_{2-x}Nd_xO_3$ samples is shown (left panel) along on *ab*-plane (viewed from top) and (right panel) along *c*-axis. The unit cell edges have been emphasized in red color.

The magnetization measurements have already shown that the samples are magnetic at room temperature, and as expected, two distinct magnetic peaks could be observed in the room temperature powder ND patterns for all the samples around $2\theta = 18.5^o$ and 20.5^o. These observations are in good agreement with the similar report on α-Fe_2O_3 thus confirming that the Nd doped Fe_2O_3 compounds tend to be of α-Fe_2O_3 magnetic structure. The overall magnetic moment per Fe (in units of Bohr magneton, μ_B) increases marginally with increasing Nd concentration (see Table 3.3). It must be noted here that we could observe moment only on Fe, and Nd is non-magnetic at room temperature.

The magnetic structure of Fe_2O_3 is shown in Fig. 3.10. As can be seen clearly from the figure, the spins are coupled ferromagnetically along the plane; however, the planes are coupled antiferromagnetically. Also, it should be noted that the arrow length denotes the moment value.

The difference in the length of the moment highlights the fact that Fe has unequal moments within the magnetic cell, exhibiting ferri-magnetic like arrangement of spins, which leads to magnetic frustration in the event of anti-parallel arrangements like in present condition. Thus the non-saturation of magnetization curves, observation of hysteresis, coercivity and distortion of polyhedra can all be explained on the basis of unequal moments on Fe, which can be due to mixed valence state of Fe.

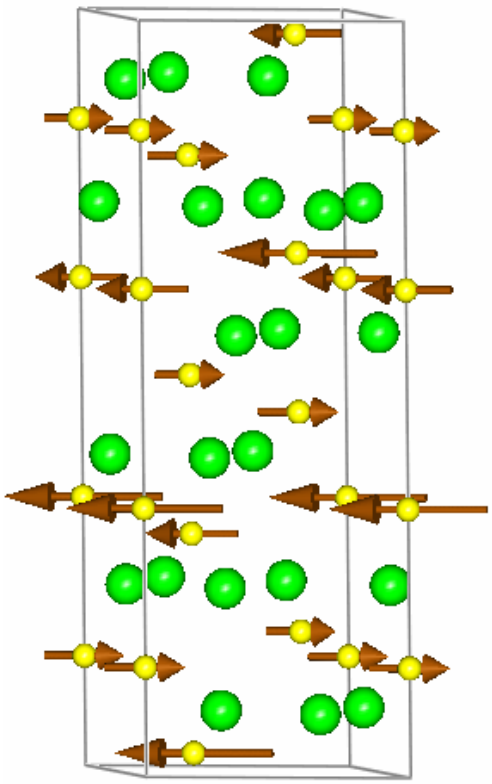

Fig. 3.10:- The Fullprof studio image of the magnetic structure of α-Fe_2O_3. The arrows are drawn on the Fe site to show the magnetic moment. Oxygen atom is shown in green (filled balls).

TABLE 3.3 Structural parameters after the Rietveld refinement of neutron-diffraction pattern of $Fe_{2-x}Nd_xO_3$ at 300 K. Atomic positions are Fe(Nd) at 12*c* (0, 0, 0.355) and O at 18*e* (0.305, 0,1/4)

Parameters		Fe_2O_3 (x = 0.0)	$Fe_{1.9}Nd_{0.1}O_3$ (x = 0.1)	$Fe_{1.7}Nd_{0.3}O_3$ (x = 0.3)	$Fe_{1.5}Nd_{0.5}O_3$ (x = 0.5)
a (Å)		5.0374(4)	5.0387(4)	5.0355(4)	5.0360(4)
c (Å)		13.7614(4)	13.7643(4)	13.7523(4)	13.7684(4)
Volume ($Å^3$)		302.42(3)	302.64(3)	301.99(3)	302.41(3)
χ^2		3.59	2.92	5.21	3.17
R_p		2.78	3.53	1.95	2.47
R_{wp}		3.63	4.43	2.51	3.18
R_{exp}		1.88	2.59	1.08	1.78
Bragg R-factor		2.76	3.51	2.58	2.97
Rf-factor		1.67	2.24	1.71	1.77
Bond Valence Sums	***Fe***	1.795	1.890	2.120	2.398
	O	1.197	1.260	1.413	1.599
Polyhedra Distortion (□ 10^{-4})	***Fe***	0.001	0.0001	0.001	0.001
	O	0.001	0.0001	0.0001	0.0001
Coordination	***Fe***	3.00	3.16	3.53	4.00
	O	2.00	2.10	2.35	2.67
D-average (Å)	***Fe***	1.949	1.949	1.947	1.948
	O	1.949	1.949	1.947	1.948
Average particle size (nm)		71	31	15	16
Magnetic R-factor (R_m)		3.13	8.05	3.91	6.51
μ_{Fe} (μ_B)		4.08	4.26	4.43	4.89

3.5. Thermo-gravimetric Analysis

The TGA curves of the as-prepared nanocrystalline sample of $Fe_{2-x}Nd_xO_3$ (NFO) series up to 900°C are shown in Fig. 3.11. The TGA curves show weight losses of 0.15%, 3.8%, 5% for sample having Nd concentration of 0.1, 0.3, and 0.5, respectively which may correspond to the adsorbed moisture in the samples. It can also be observed from the curve that sample having 0.5, 0.3 and 0.1 concentration of Nd stabilizes at 550°C, 600°C and 700°C repectively. Hence, sample having maximum concentration of Nd stablizes more quickly as compared to sample having low concentration of Nd. Thus, it can be concluded that Nd-substitution strengthens the bonding between Fe and O which can also be observed from neutron diffraction data (see table 3.3).

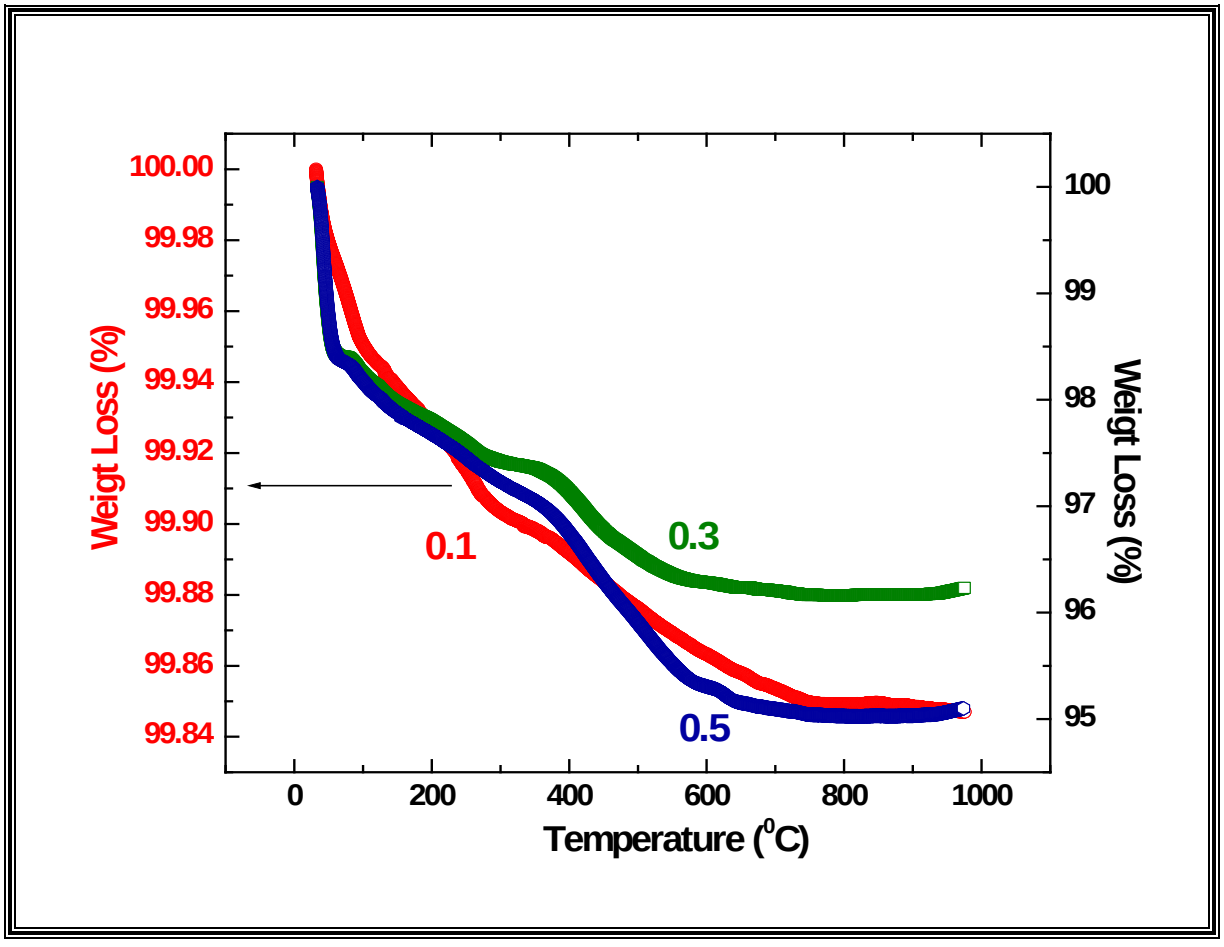

Figure 3.11: TGA curves for: (a) $Nd_{0.1}Fe_{1.9}O_3$ (b) $Nd_{0.3}Fe_{1.7}O_3$ and (c) $Nd_{0.5}Fe_{1.5}O_3$ respectively.

REFRENCES

1. A. H. Hill, F. Jiao, P. G. Bruce, A. Harrison, W. Kockelmann, and C. Ritter, *Chem. Mater.* **20** (2008) 4891.
2. Cullity, B.D.; C.D. Graham (2008). *Introduction to Magnetic Materials*. Wiley-IEEE. ISBN 0471477419.
3. C. Rath, K. K. Sahu, S. D. Kulkarni, S. Anand, S. K. Date, R. P. Das, N. C. Mishra, Appl. Phys. Lett. 75 (1999) 4171.
4. Franz Bødker, Mikkel F. Hansen, Christian Bender Koch, Kim Lefmann, S. Mørup, Phys. Rev B. 61 (2000) 6826.
5. E. del Barco, M. Duran, J. M. Hernandez and J. Tejada, Phys. Rev B. 65 (2002) 052404.
6. Stephen Blundell, Magnetism in Condensed Matter, Oxford University Press (2001).

Chapter 4

Summary

In the present work, we have synthesized nanocrystalline samples of $Fe_{2-x}Nd_xO_3$ (NFO), where x= 0.0, 0.1, 0.3 and 0.5 respectively using combustion method. All the four compounds follow the hematite (α-Fe_2O_3) structure and exhibited rhombohedral symmetry having space group R-3c. In fact TGA/DSC studies also confirms that combustion of the samples is complete and no other species is present in the samples

The M(H) curves at room temperature showed a superparamagnetic nature with very small hysteresis due to agglomeration. Smaller the size of the particles larger is the non-saturation field. The sample with larger average size or larger agglomerates has large value of H_c compared to the samples with smaller average size particle since they experience the external field as well as the stray fields of neighboring particles. The blocking temperature, obtained from M(T) measurements, decreases with increasing Nd concentration which signifies the dilution of magnetism.

Neutron Diffraction (ND) experiments at room temperature showed that the overall magnetic moment per Fe (in units of Bohr magneton, μ_B) increases marginally with increasing Nd concentration. One of the interesting observation can also be seen that with the increase in the Nd doping till x=0.3 the average particle size decreases with a very small increase in size for x = 0.5. We believe that to some extent inclusion of Nd in α-Fe_2O_3 helps the material to restrict the particle size or from agglomeration. It is also possible that Nd substitution for Fe leads to magnetic frustration arising out of unequal moments on Fe or by driving Fe into mixed valence state. For better understanding of these observations, a detailed low temperature neutron diffraction study is planned.

ANNEXURE

Studies on $Gd_xFe_{2-x}O_3$ (x=0.1) nanoparticles synthesized through Sol-Gel method

1. Introduction

The Sol-Gel method is a widely used method for in a number of technologies [1]. As the name suggests sol-gel involves two types of materials or components, ‘sol’ and ‘gel’. Sol-gels are known since the time when M. Ebelman synthesized them in 1845. However it is only last one or two decades that considerable interest in it, both in scientific and industrial field, has generated due to realization of several advantages one gets as compared to some other techniques. First of all sol-gel formation process is usually a low temperature process. This means less energy consumption and less pollution too. In some cases sol-gel can be an economical route, provided precursors are not very expensive. Some of the benefits like getting unique materials such as aerogels, zeolites, ordered porous solids by organic-inorganic hybridization are unique to sol-gel process. It is also possible to synthesize nanoparticles, nanorods etc. using this method.

Sols are solid particles in liquid. They are thus a subclass of colloids. Gels are nothing but a continuous network of particles with pores filled with liquid. A sol-gel process involves formation of ‘sols’ in a liquid and then connecting the sol particles to form a netwok. By drying the liquid, it is possible to obtain powders, thin films or even monolithic solid. Sol-gel method is particulary useful to synthesize ceramics or metal oxide although sulphides, borides and nitrides are possible.

Synthesis of sol-gel in general involves hydrolysis of precursors, condensation followed by polycondensation to form particles, gelation and drying process by various routes. Precurosrs are to be chosen so that they have a tendency to form gels. Both alkoxides and metal salts can be used. By polycondensation (i.e. many hydrolyzed units coming together by removal of some atoms from small molecules like OH) sols are nucleated and ultimately sol-gel is formed [2-4].

2. Experimental

For synthesis of $Gd_{0.1}Fe_{1.9}O_3$ nanoparticles, Iron nitrate nonahydrate, $Fe(NO_3)_3.9H_2O$; and Gadolinium nitrate hexahydrate, $Gd(NO_3)_3.6H_2O$ were taken in stochiometric ratios and ground to make it homogenous mixture. The precursor powders were dissolved in distilled water. In another beaker add stochiometric amount of citric acid in minimum amount of ethylene glycol. Ethylene glycol is used for polycondensation while citric acid is used to increase the surface area of the particles and thus it prevents agglomeration.

Add citric acid drop wise (preferably) into the solution of the nitrates with continuous stirring. The pH value of 2-3 was maintained using ammonia. Let the solution stir at around 50-60^{0}C continuously and the solution will itself become viscous with time and will eventually dry up to form powder. The final powder is homogenized and further calcined at 400 ^{o}C for 2 hours and put for further characterization.

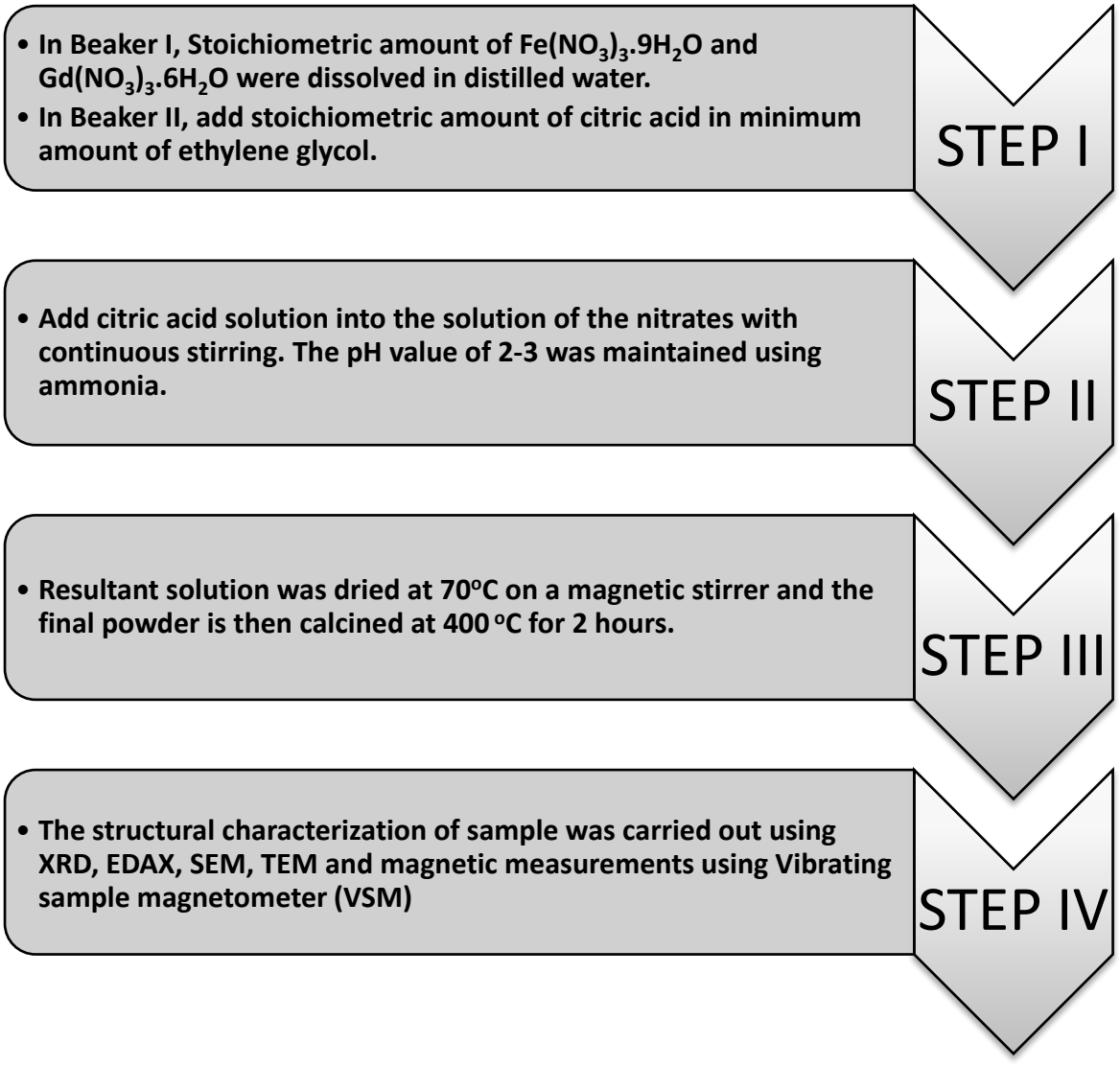

Fig 1:- Flow chart for the synthesis of $Gd_{0.1}Fe_{1.9}O_3$ nanoparticle by sol-gel method**.**

3. RESULTS

3.1. X-Ray Diffraction (XRD)

Figure 2 shows the XRD patterns of $Gd_{0.1}Fe_{1.9}O_3$ sample and it indicates that the compounds of this series forms in the hematite (α-Fe_2O_3) structure. The sample exhibited rhombohedral symmetry having R-3c space group. The XRD has two following features:

(i) The highest intensity peak was observed at 35.61^o.

(ii) An extra peak (shown by * mark in figure) is present besides the peaks of α-Fe_2O_3. This peak shows that an impurity phase is present possibly of γ- Fe_2O_3.

The reflection from the 110 lattice phase was used to estimate the average crystallite size by applying the Scherrer model, this can be written as

$$d = 0.9\lambda/\beta\cos\theta,$$

where λ = 1.54 nm for the CuK_α line, d is the crystallite diameter,
β is the full width at half maximum in radians and 'θ' is the peak position.

Applying this formula to the spectrum shown in gives an average **crystallite size of 25 nm**.

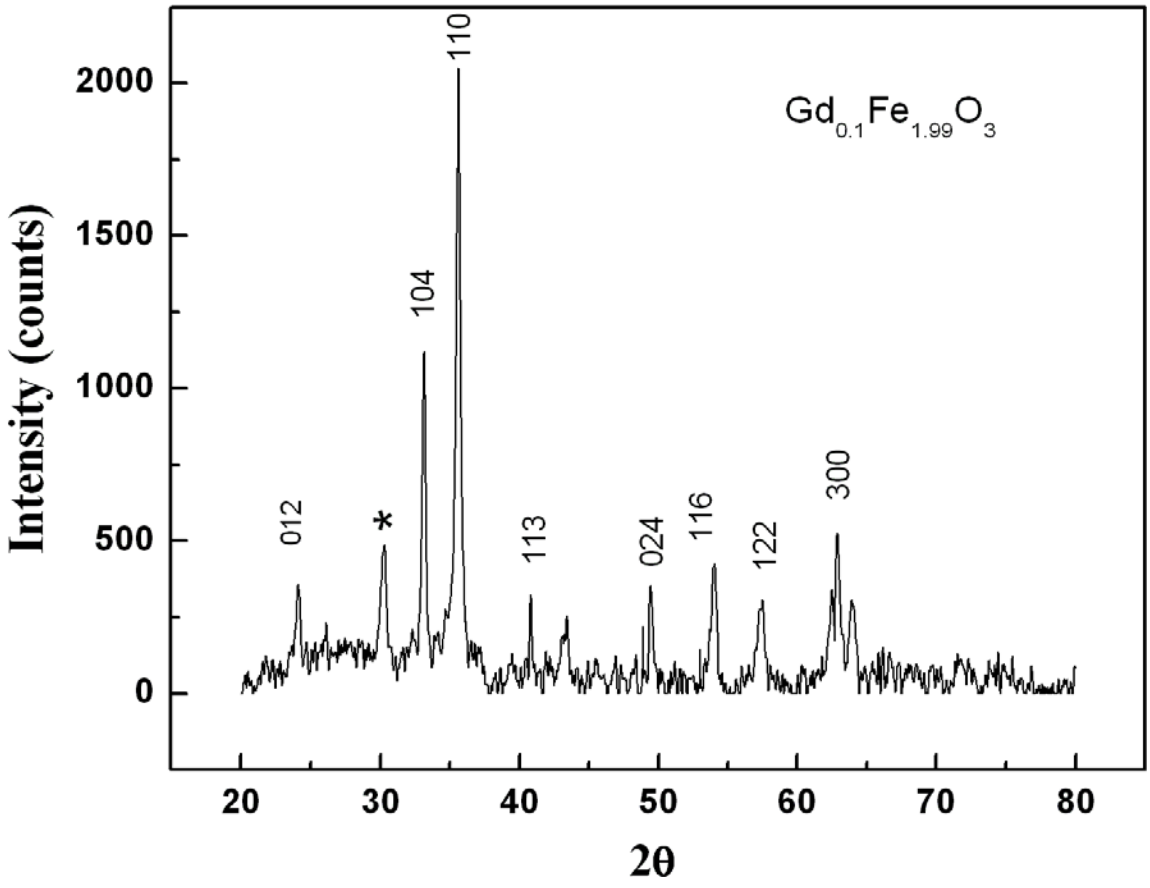

Fig 2: XRD for the $Gd_{0.1}Fe_{1.9}O_3$ nanoparticle.

3.2. Energy Dispersive Spectroscopy (EDAX)

The EDAX of the sample shows that the sample contains the following elements in respective weight percent. Hence no impurity is present in sample and it contains all the desired elements.

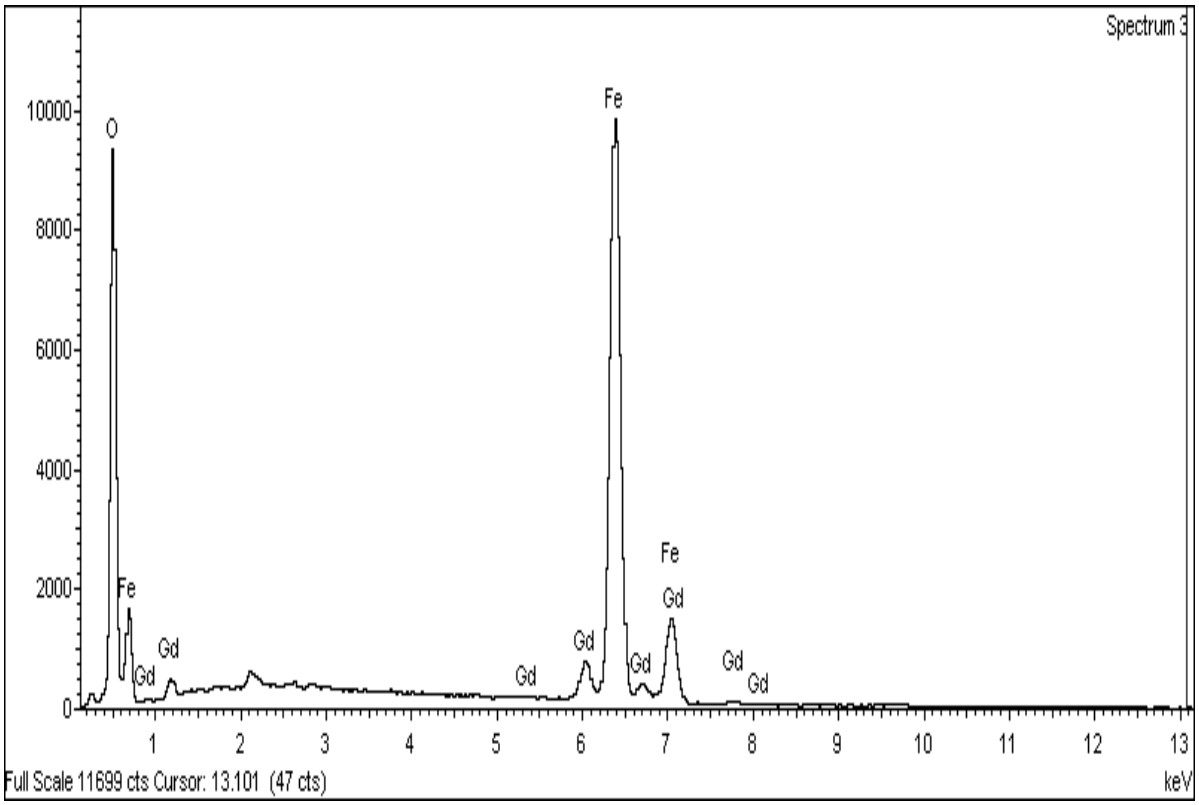

Fig3: EDAX for the $Gd_{0.1}Fe_{1.9}O_3$ nanoparticle.

Element	Wt.%	Atomic%
O	29.39	61.27
Fe	61.69	36.84
Gd	8.91	1.89

3.3. Scanning Electron Microscopy (SEM)

To visualize the images of the particles of the prepared material, SEM has been performed. SEM images demonstrate that the particles have wide size distribution. Large agglomeration of the nanoparticles is clearly observed. In fact Fe_2O_3 is very well known for the formation of agglomerated nanoparticles because of their magnetic nature [5].

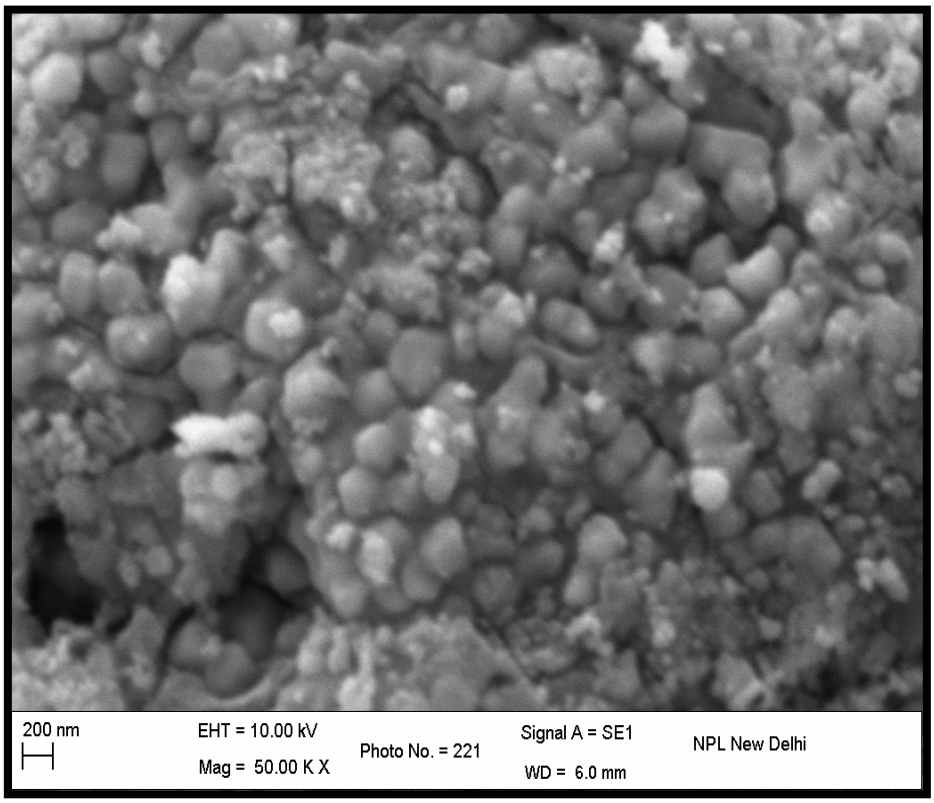

Fig 4:- SEM Image of Gd doped iron oxide nanoparticle

3.4. Transmission Electron Microscopy (TEM)

TEM image confirmed the nanosized of particles. From TEM image the particles were calculated in the range of 20-25 nm which is in good agreement with the particle size calculated from XRD. The d-value from TEM is 0.294nm which also confirmed the material formed is of α-Fe_2O_3 phase.

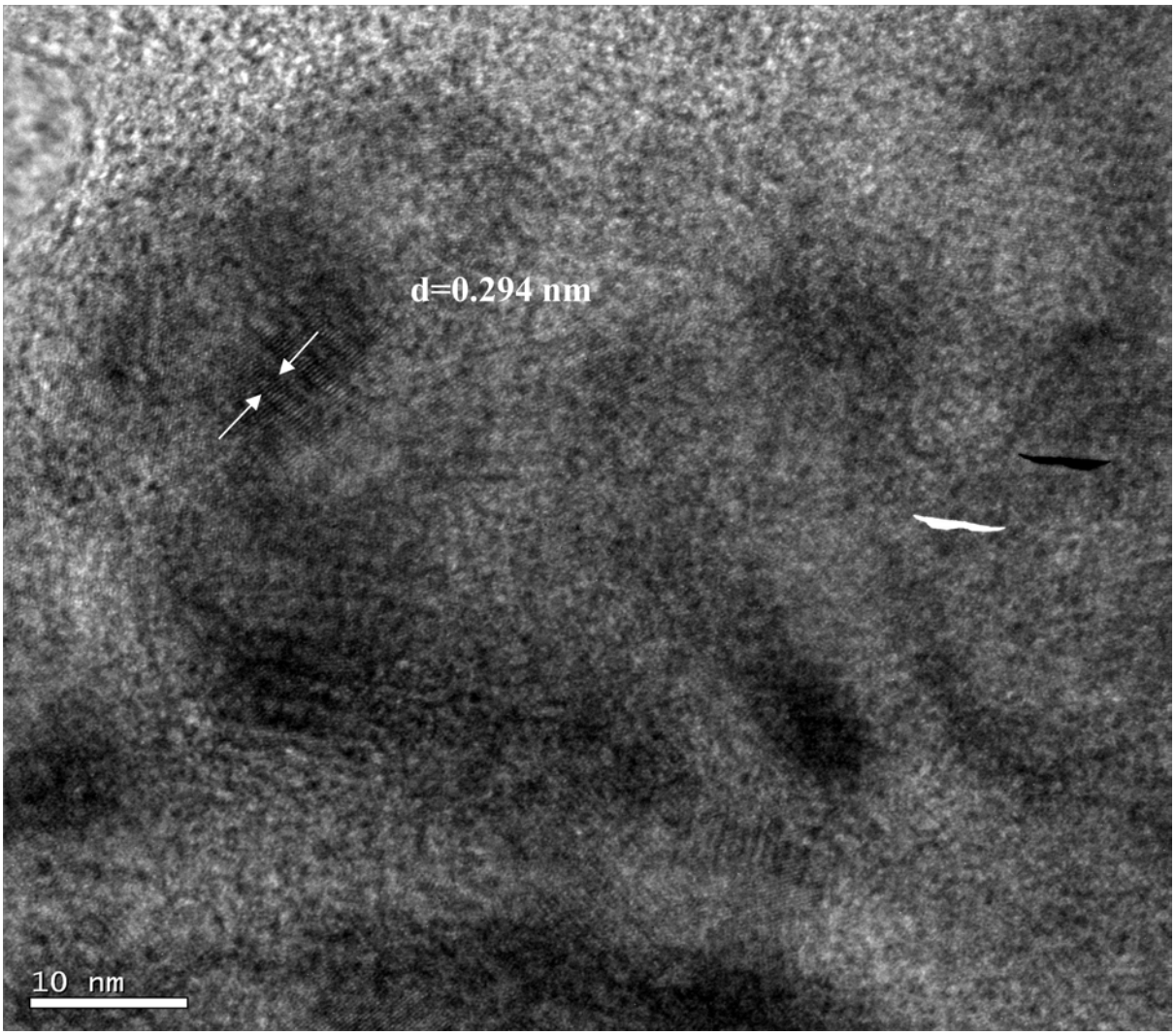

Fig 5:- TEM Image of Gd doped iron oxide nanoparticle.

3.5. Magnetization

Magnetization as a function of applied field was performed at room temperature for nanocrystalline $Gd_{0.1}Fe_{1.9}O_3$ sample with a symmetric shape about the center as shown in Fig.6. We observe from TEM that we do have the particles with the nano sizes. But it can also be seen from the curve that there is a very small hysteresis which concluded that the samples consists not only nanosized particles but also have agglomerated particles that contribute to the hysteresis behavior. However, particles are also showing superparamagnetic character because of the nano size particles present in the system.

Coercivity (H_c) in the material was observed due to agglomerated particles as they experience the external field as well as the stray fields of neighboring particles [6]. The smaller remnant magnetization for $Gd_{0.1}Fe_{1.9}O_3$ nanoparticles is probably associated with the fine spherical shape of the hematite nanoparticles, since the remnant magnetization is strongly dependent upon the particle shape [7].

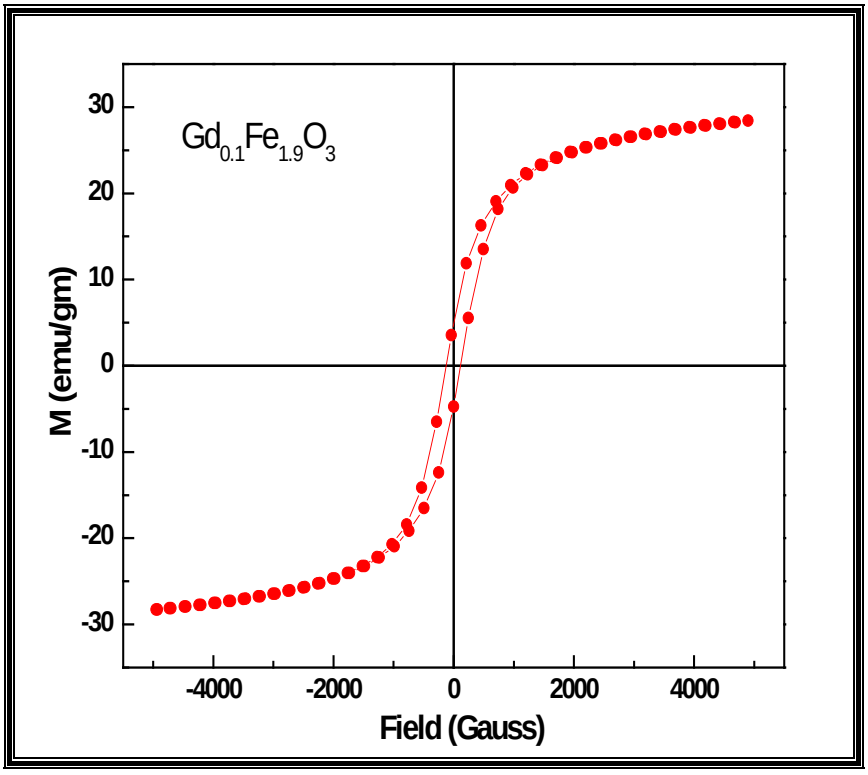

Fig 6:- Magnetization as a function of field of $Gd_{0.1}Fe_{1.9}O_3$ sample.

REFERENCES

1. Basic Priciples of colloid Science by D.H. Everett, Royal Society of Chemistrt (1998).
2. Sol-Gel Science: The Physics ans Chemistry of Sol-Gel Processing by C. Jeffrey Brinker and J.W. Scherer, Academic Press, Boston (1990).
3. Fundamental Principles of Sol-Gel Technology by R.W. Jones, The Institute of Metals (1989).
4. Introduction to Sol-Gel Processing by Alan C. Pierre, Kluwer Academic Publisher, Boston (1998).
5. Franz Bødker, Mikkel F. Hansen, Christian Bender Koch, Kim Lefmann, S. Mørup, Phys. Rev B. 61 (2000) 6826.
6. C. Rath, K. K. Sahu, S. D. Kulkarni, S. Anand, S. K. Date, R. P. Das, N. C. Mishra, Appl. Phys. Lett. 75 (1999) 4171.
7. L. Li, G. Li, R.L. Smith Jr., H. Inomata, Chem. Mater. 12 (2000) 3705.